Automatic Spectral-Rule-Based Preliminary Classification of Radiometrically Calibrated SPOT-4/-5/IRS, AVHRR/MSG, AATSR, IKONOS/QuickBird/OrbView/GeoEye, and DMC/SPOT-1/-2 Imagery—Part I: System Design and Implementation

Andrea Baraldi, Laurent Durieux, Dario Simonetti, Giulia Conchedda, Francesco Holecz, and Palma Blonda, *Member, IEEE*

***Abstract*—To date, the automatic or semiautomatic transformation of huge amounts of multisource multiresolution spaceborne imagery into information still remains far below reasonable expectations. The original contribution of this paper to existing knowledge on the development of operational automatic remote sensing image understanding systems (RS-IUSs) is fourfold. First, existing RS-IUS architectures are critically revised. In this review section, the two-stage stratified hierarchical RS-IUS model, originally proposed by Shackelford and Davis, is identified as a subclass of the parent class of multiagent hybrid systems for RS image understanding, which is potentially superior to the two-stage segment-based RS-IUS architecture that is currently considered the state-of-the-art in commercial RS image-processing software toolboxes. Second, this paper highlights the degree of novelty of an operational automatic near-real-time well-posed model-driven application-independent per-pixel Landsat-like spectral-rule-based decision-tree classifier (LSRC) recently presented in RS literature. Third, five original downscaled implementations of the LSRC system are proposed to be input with a multispectral image whose spectral resolution overlaps with, but is inferior to, Landsat's. These five downscaled LSRC implementations are identified as the Satellite Pour l'Observation de la Terre-like SRC, the Advanced Very High Resolution Radiometer-like SRC, the Advanced Along-Track Scanning Radiometer-like SRC, the IKONOS-like SRC, and the Disaster Monitoring Constellation-like SRC, respectively. LSRC, together with its five downscaled implementations, called the integrated SRC system of systems, is eligible for use as the automatic pixel-based preliminary classification first stage of a two-stage stratified hierarchical RS-IUS instantiation. Fourth, to sustain the feasibility of the new downscaled LSRC implementations, a novel vegetation spectral index is introduced and discussed. In Part II of this paper, experimental results are presented and discussed for the entire SRC family of classifiers.**

***Index Terms*—Decision-tree classifier, image classification, inductive and deductive inference, prior knowledge, radiometric calibration, remote sensing (RS).**

I. Introduction

THE POTENTIAL of Earth observation (EO) from space for the monitoring of the Earth's environment and the detection of its temporal variations at geographic extents ranging from local (areas up to 100 000 km^2) to regional (areas roughly between 100 000 and 1 000 000 km^2), continental, and global scales is well known by user communities involved with urban-growth assessment and planning, intelligence/surveillance applications for national security and defense purposes, ecosystem management, watershed protection, water balance calculations, risk management, and global change [1]–[4].

The expected impact of remote sensing (RS) imagery upon the general public has increased after the recent announcement by the Group on Earth Observations[1] (GEO) that scientists and decision makers around the world will soon have unrestricted

Manuscript received August 1, 2008; revised December 31, 2008 and July 1, 2009. First published December 4, 2009; current version published February 24, 2010.

A. Baraldi was with the European Commission Joint Research Center (EC-JRC), 21020 Ispra, Italy. He is now with Baraldi Consultancy in Remote Sensing, 40129 Bologna, Italy (e-mail: andrea6311@gmail.com).

L. Durieux was with the EC-JRC, 21020 Ispra, Italy. He is now with the Institut de Recherché Pour le Développement, Maison de la Teledetection, 34093 Monpellier Cedex 05, France (e-mail: Laurent.durieux@ird.fr).

D. Simonetti is with the EC-JRC, 21020 Ispra, Italy (e-mail: dario.simonetti@ext.jrc.ec.europa.eu).

G. Conchedda is with the European Commission, Brussels, Belgium (e-mail: giulia.conchedda@jrc.it).

F. Holecz is with Sarmap s.a., 6989 Purasca, Switzerland (e-mail: fholecz@sarmap.ch).

P. Blonda is with the Istituto di Studi sui Sistemi Intelligenti per l'Automazione, Consiglio Nazionale delle Ricerche, 70126 Bari, Italy (e-mail: blonda@ba.issia.cnr.it).

Color versions of one or more of the figures in this paper are available online at http://ieeexplore.ieee.org.

Digital Object Identifier 10.1109/TGRS.2009.2032457

[1]GEO was launched in response to calls for action by the 2002 World Summit on Sustainable Development and by the Group of Eight leading industrialized countries [5]. GEO provides a framework for the coordination of efforts and strategies to address common goals in EO. It comprises a voluntary partnership of 77 governments and the EC, in addition to 56 intergovernmental, international, and regional organizations with a mandate in EO or related issues that have been recognized as Participating Organizations. In 2005, GEO launched a "ten-year implementation plan" to establish its visionary goal of a Global Earth Observation System of Systems (GEOSS) [6].

access at no charge to the Landsat archive, the world's most extensive collection of continuously acquired RS spaceborne imagery [1], [5], [6]. This news followed the decision of the China–Brazil Earth Resources Satellite (CBERS) to distribute its images free of charge starting from the year 2007. In turn, the European Union (EU) announced a free data policy for the Sentinel-2/-3 satellites whose launch is scheduled starting from 2012.

While the cost-free access to large-scale low-spatial-resolution (SR) (LR, above 40 m) and medium-SR (MR, from 40 to 15 m) spaceborne image databases is becoming a reality, the demand for high-SR (HR, between 15 and 5 m) and very high SR (VHR, below 5 m) commercial satellite imagery has continued to increase in terms of both quantity and quality of data, which has boosted the rapid growth of the commercial VHR satellite industry [4].

These multiple drivers make urgent the need to develop operational satellite-based measurement systems suitable for automating the quantitative analysis of RS imagery. This objective has been a traditional goal of the RS community involved with global land cover and land cover change programs, such as the Land Use and Land Cover Change (LUCC) project and the National Aeronautics and Space Administration (NASA) Land Cover and Land Use Change (LCLUC) program[2] [2, pp. 451, 452]. The same visionary goal is envisaged under ongoing international programs such as the following: 1) the Global Earth Observation System of Systems (GEOSS), conceived by GEO [5], [6], that requires harmonization and interoperability of EO data and derived information products generated from a variety of sources at all scales—global, regional, and local—and 2) the Global Monitoring for the Environment and Security (GMES), an initiative led by the EU in partnership with the European Space Agency (ESA), whose aim is to guarantee the sustainability of integrated operational services for EU security and environmental monitoring based on EO data from multiple sources (satellite, airborne, and *in situ*) and synergistic data products [7], [8].

Unfortunately, to date, the automatic or semiautomatic transformation of huge amounts of multisource multiresolution RS imagery into information still remains far below reasonable expectations [9]. This well-known opinion by Zamperoni may explain why, for example, the percentage of data downloaded by stakeholders from the ESA EO databases is estimated at about 10% [10].

In RS common practice, insufficient spaceborne image mapping capability may be due to two main factors.

1) Existing scientific and commercial RS image understanding systems (RS-IUSs), including those which recently gained noteworthy popularity such as eCognition [11] and the Atmospheric Correction for satellite imagery (ATCOR3) [12], score low in operational performance which encompasses the following [13]–[15]: a) ease of use (degree of automation; when a data-processing system is automatic, it requires no user-defined parameter to run; hence, its ease of use is unsurpassed); b) effectiveness (e.g., classification accuracy); c) efficiency (e.g., computation time and memory occupation); d) economy (cost; it increases monotonically with manpower, e.g., the manpower required to collect scene-specific training samples); e) robustness to changes in input parameters; f) robustness to changes in the input data set; g) maintainability/scalability/reusability to keep up with the users' changing needs; and h) timeliness (defined as the time span between data acquisition and product delivery to the end user; it increases monotonically with manpower). For example, a low operational performance measurement may explain why the literally hundreds of so-called novel low (subsymbolic)- and high (symbolic)-level image-processing algorithms presented each year in scientific literature typically have a negligible impact upon commercial RS image-processing software toolboxes [9].
2) The increasing rate of collection of RS data of enhanced spatial, spectral, and temporal quality outpaces the capabilities of both manual inspection and inductive machine learning from supervised (labeled) EO data. The cost, timeliness, quality, and availability of adequate reference (training/testing) data sets derived from field sites, existing maps, and tabular data are currently considered the most limiting factors on RS data product generation and validation [2].

It is well known that one key to operational performance is automating operations [14], [15]. In automating a data-processing system, *necessary, although not sufficient, conditions* are for input data to be [16] as follows.

1) Well behaved, namely, every input variable is expressed in a community-agreed unit of measure and belongs to a known domain of variation. In particular, EO-sensor-derived data are well behaved when they are as follows.
   a) Radiometrically calibrated, i.e., dimensionless digital numbers (DNs) are transformed into a radiometric unit of measure in agreement with the Quality Assurance Framework for Earth Observation data (QA4EO) initiative, led by the Committee of Earth Observations[3] (CEOS) Working Group on Calibration

[2]The LUCC project was formally inaugurated by a 1996 Open Science Meeting in Amsterdam as an initiative by the International Geosphere–Biosphere Program–International Social Science Council working group [2, p. 3]. The LUCC core project will continue through 2005. The NASA LCLUC program started in 2003 to contribute to the U.S. Climate Change Science Program 2003 by developing interdisciplinary science with a high degree of societal relevance, such as global environmental change, Earth systems, sustainability, environment development, and conservation, among others [2, pp. 8, 18].

[3]CEOS was created in 1984 in response to a recommendation by the Economic Summit of Industrialized Nations Working Group on Growth, Technology, and Employment's Panel of Experts on Satellite Remote Sensing [99]. This group recognized the multidisciplinary nature of satellite EO and aims at optimizing benefits of spaceborne EO through cooperation among its participants in mission planning and in the development of compatible data products, formats, services, applications, and policies. CEOS became the space arm of GEO in 2006. In that capacity, CEOS is playing an active role in the establishment of GEOSS. CEOS members are, among others: Agenzia Spaziale Italiana (ASI), British National Space Centre (BNSC), Centre National d'Etudes Spatiales (CNES), Deutsches Zentrum für Luft- und Raumfahrt (DLR), European Commission (EC), ESA, European Organization for the Exploitation of Meteorological Satellites (EUMETSAT), NASA, National Oceanic and Atmospheric Administration (NOAA), Canadian Space Agency (CSA), Instituto Nacional de Pesquisas Espaciais (INPE) and Indian Space Research Organization (ISRO) .

and Validation[4] (WGCV) in the context of the GEOSS program [17]. For example, an appropriate coordinated program of calibration and validation (Cal/Val) activities throughout all stages of a spaceborne mission, from sensor build to end of life, is considered mandatory by the QA4EO initiative [17].

b) Geometrically corrected, i.e., projected onto a community-agreed terrestrial reference system.

c) Validated, i.e., provided with quantitative, unequivocal, and traceable measures of geometric and radiometric quality and uncertainty in agreement with the QA4EO guidelines [17].

2) Well understood by the system developer, namely, every input data source is provided with a clear physical meaning and with a community-agreed data format.

To summarize, the first step in automating RS-IUSs should be the achievement of the aforementioned necessary conditions for input data. According to machine learning [18], computer vision [19], RS literature [16], [20] and common sense (synthesized by the expression "garbage in, garbage out"), this achievement would augment the degree of prior knowledge of an RS-IUS required to complement the intrinsic insufficiency (ill posedness) of image features (refer to further Section II-A). On the contrary, most (if not all) existing commercial and scientific RS-IUSs do not require RS images to be radiometrically calibrated and validated in terms of unequivocal geometric and radiometric quality. As a consequence, these RS-IUSs adopt a manual or, at best, semiautomatic data understanding approach on a scene-by-scene basis (since one scene may represent, for example, apples while a contiguous or overlapping scene may represent, for example, oranges) [23], [24].

The original contribution of this paper to existing knowledge on the development of operational automatic RS-IUSs is fourfold.

1) A critical analysis of existing RS-IUS architectures and implementation strategies provides this paper with a significant survey value [11], [21], [25], [26].

2) The recently proposed operational automatic near-real-time well-posed model-driven application-independent per-pixel Landsat-like spectral-rule-based decision-tree classifier (LSRC) is discussed to highlight its degree of novelty [20], [27]. In agreement with the QA4EO guidelines, LSRC requires as input a seven-band Landsat-like image radiometrically calibrated into top-of-atmosphere (TOA) reflectance (TOARF) or surface-reflectance values, the latter being an ideal (atmospheric-noise-free) case of the former.

3) Five original downscaled implementations of the LSRC system are proposed to be input with a radiometrically calibrated multispectral (MS) image whose spectral resolution overlaps with, but is inferior to, Landsat's. In line with the vision of an integrated multisource EO system of systems, such as GEOSS [17], the pixel-based LSRC system, together with its five downscaled implementations, hereafter identified as the integrated SRC system of classifiers, can be considered as follows: a) sensor independent, i.e., it employs as input an MS image acquired by almost any of the existing or future planned satellite optical imaging sensors and b) sensor resolution independent, i.e., it works at the sensor (pixel) resolution.

4) To justify the scalability of LSRC to MS imaging sensors featuring a spectral resolution inferior to Landsat's, spectral indexes found in existing literature are surveyed, and a novel vegetation spectral index is proposed and discussed.

To reach its multiple objectives, this paper is organized as follows. Section II surveys related works on the subjects of 1) image understanding as an inherently ill-posed problem, 2) RS image radiometric calibration and atmospheric correction, 3) architectures and implementations of existing RS-IUSs, and 4) the degree of novelty of the fully automated LSRC approach. Section III presents five original downscaled versions of LSRC. In RS common practice, limitations on the applicability domain of the integrated SRC system of systems are encountered when the radiometric correction of RS data for sensor gain and offset effects is not reliable. Although it is rarely the subject of concern in the RS community, this issue is thoroughly discussed in Section IV. Another limitation on the applicability domain of the integrated SRC system stems from a theoretical inadequacy of the spectral resolution of VHR optical sensors to cope with the dichotomous (one-class) vegetation/nonvegetation classification problem. This subject is investigated in Section V where a novel greenness index is proposed. Conclusions are reported in Section VI. In Part II of this paper, experimental results are presented and discussed for the entire SRC family of classifiers.

II. Related Works and Definitions

In this section, the inherent ill posedness of the image understanding problem is highlighted while concepts related to RS data radiometric calibration and atmospheric correction relevant to the development of operational automatic RS-IUSs are discussed. In addition, starting from the customary distinction between a model and the algorithm used to identify it [28], this section adopts the well-known *divide-and-conquer* problem-solving paradigm [29] to review the model (architecture) design principles and inference (learning) mechanisms adopted by existing RS-IUSs whose taxonomy comprises three major families: 1) multiagent hybrid RS-IUSs; 2) two-stage segment-based RS-IUSs; and 3) two-stage stratified hierarchical RS-IUSs. Finally, this section examines the degree of novelty of the automatic LSRC system eligible for use as the preliminary pixel-based classification first stage of a two-stage stratified hierarchical RS-IUS instantiation.

[4]Initiated in 1984, the CEOS WGCV pursues activities to coordinate, standardize, and advance the calibration and validation of EO missions and their data in the conviction that the space agencies and commercial satellite data providers should present EO data in a way that would ensure the possibility of comparing sensors and products [100]. Thus, CEOS WGCV, in partnership with the Institute of Electrical and Electronics Engineers, was the natural GEO choice to carry out the task of developing an international QA4EO initiative in the context of GEOSS. Started in two GEO/CEOS workshops held in 2007 and 2008, the ongoing QA4EO initiative is conceived as an international EO Cal/Val community-derived process to establish an international QA framework to facilitate the harmonization and interoperability of EO data, metadata, derived information products, and operations required to achieve them [17].

A. Ill-Posed Image Understanding Problem

Any imaging sensor projects a [three-dimensional (3-D)] scene onto a [two-dimensional (2-D)] image so that the main role of a biological or artificial IUS is to backproject the information in the image domain to that in the scene domain, i.e., to associate subsymbolic (2-D) image features with symbolic (3-D) objects in the scene (e.g., buildings and roads) [19], [30]–[32]. There is a well-known information gap between symbolic information in the (3-D) scene and subsymbolic information in the (2-D) image due to dimensionality reduction, e.g., occlusion phenomena. This is called the *intrinsic insufficiency* of image features [19]. In other words, the problem of image understanding is inherently ill posed and, consequently, very difficult to solve [19].

This information gap is the same gap existing between (subsymbolic, sensory, instantaneous, numerical, quantitative, absolute, and asemantic) sensation and (symbolic, linguistic, qualitative, vague, abstract, persistent, and stable) perception, which has been thoroughly investigated in both philosophy and psychophysical studies of perception. In practice, "we are always seeing objects we have never seen before at the sensation level, while we perceive familiar objects everywhere at the perception level" [19].

This information gap is also related to the inherent ill posedness of inductive inference. Starting from classical philosophy to end up with machine learning, it is well known that the general notion of inference (learning) comprises two types of learning mechanisms known as "induction [i.e., progressing from particular (e.g., training data) to general cases (e.g., estimated dependence or model)]," therefore called bottom–up, fine to coarse, data driven, or learning by example, and "deduction [i.e., progressing from general (e.g., model) to particular cases (e.g., output values)]," therefore called top–down, coarse to fine, model driven, or learning by rule [33]. In particular, "induction amounts to forming generalizations from particular true facts. This is an inherently difficult (ill-posed) problem, and its solution requires *a priori* knowledge in addition to data" [33, p. 39].

To summarize, the ill-posed primary objective of any biological or artificial IUS is to construct one or more plausible symbolic structural descriptions of the (3-D) scene depicted in a (2-D) image by means of a combination of inductive (bottom–up, fine to coarse, data driven, and learning by example) and deductive (top–down, coarse to fine, model driven, and learning by rule) inference mechanisms capable of filling in the well-known information gap between 1) the intrinsically insufficient subsymbolic (sensory, quantitative, and asemantic) information (features) extracted from the image, namely, points and regions or region boundaries, i.e., edges, and 2) symbolic (linguistic, qualitative, abstract, and semantic) persistent (stable) percepts (concepts, terms, classes of (3-D) objects, (3-D) object models, or templates) representing (prior) knowledge about the real (3-D) world, called the *world model* [19].

B. Radiometric Calibration and Atmospheric Correction

In spite of being regarded as common knowledge in the RS community, the issue of radiometric calibration, i.e., the transformation of dimensionless DNs into a physical unit of measure related to a community-agreed radiometric scale, is often neglected in literature and surprisingly ignored by RS scientists, practitioners, and institutions involved with common practice including large-scale spaceborne image mosaicking and mapping [24], [34]–[36]. Since LSRC (discussed in further Section II-D) requires as input an MS image that is radiometrically calibrated into TOARF or surface-reflectance values, the latter being an ideal (atmospheric-noise-free) case of the former, the subject of radiometric calibration is further developed in this section to make this paper self-contained.

Acknowledged by a significant portion of existing literature, such as the international QA4EO guidelines (see Section I), radiometric calibration achieves the following objectives.

1) It ensures the harmonization and interoperability of multisource observational data and derived products required by international programs such as the ongoing GEOSS and GMES projects [5], [6], [8].
2) It makes RS data well behaved and well understood [34], which paves the way for automating the quantitative analysis of EO data [26], [37], as underlined by this paper (refer to Sections I and II-D).

Radiometric calibration comprises a sequence of three steps.

1) Linear transformation of DNs into TOA radiance (TOARD) values ≥ 0 [12]. This first calibration step is also known as *absolute radiometric calibration* [38].
2) Nonlinear transformation of TOARD values into TOARF values belonging to range [0, 1].
3) When atmospheric effects are taken into account, transformation of either TOARD or TOARF values into surface radiance L values ≥ 0 or surface-reflectance ρ values belonging to range [0, 1], respectively. Unfortunately, the problem of atmospheric correction is typically ill or poorly posed. Consequently, it is very difficult to solve and requires user's supervision to make it better posed [12].

These three preprocessing steps are discussed hereafter.

Absolute radiometric calibration [38] is the linear transformation of a pixel value $DN(n,b) \geq 0$, with $n = 1, \ldots, N$ and $b = 1, \ldots, Bnd$, where N is the total number of pixels and Bnd is the number of spectral channels (bands), into a $TOARD(n,b)$ value ≥ 0, expressed in a radiometric unit of measure, either $[\mathrm{W}/(\mathrm{m}^2 \times \mathrm{sr} \times \mu\mathrm{m})]$ (e.g., in the Landsat, Satellite Pour l'Observation de la Terre (SPOT), Advanced Spaceborne Thermal Emission and Reflection Radiometer (ASTER), and QuickBird optical sensors) or $[\mathrm{mW}/(\mathrm{cm}^2 \times \mathrm{sr} \times \mu\mathrm{m})]$ (e.g., in the IKONOS and Indian Remote Sensing Satellite (IRS) optical sensors) [12], as a function of the gain $G(b) \geq 0$ and offset $O(b) \geq 0$ calibration parameters for band $b = 1, \ldots, Bnd$, to be retrieved from the RS image metadata file. For example, in the case of SPOT-1/-5 imagery [39]

$$0 \leq TOARD(n,b) = [DN(n,b)/G(b)] + O(b), \quad n = 1, \ldots, N;\ b = 1, \ldots, Bnd \quad (1.1)$$

where the gain and offset parameters are identified, respectively, as "⟨PHYSICAL_GAIN⟩" and "⟨PHYSICAL_BIAS⟩"

in the SPOT metadata digital image map (DIMAP) file format.

The model for obtaining dimensionless true terrain reflectance $\rho(n, \lambda, t, lat, long) \in [0, 1]$ from the spectral radiance at the sensor's aperture $TOARD(n, \lambda)$ may be expressed as follows [40]:

$$\rho(n, \lambda, t, lat, long) = \frac{\pi \cdot d(t)^2 \cdot \left(\frac{TOARD(n,\lambda) - L_a(\lambda)}{\tau_{\mathrm{uw}}(\lambda)} \right)}{ESUN(\lambda) \cdot \cos\left(\theta_z(t, lat, long)\right) \cdot \tau_{\mathrm{dw}}(\lambda) + E_d(n, \lambda)} \in [0, 1], \quad n = 1, \ldots, N \tag{1.2}$$

where λ is the electromagnetic wavelength, $(lat, long)$ is the pixel position in geographic coordinates, and $d(t)$ is the Earth–Sun distance in astronomical units to be interpolated from values found in literature as a function of the viewing day and time t transformed into a Julian day value in the range {1, 365} such that $d(t)$ approximately belongs to range $1 \pm 3.5\%$ [41]. $L_a(\lambda) \geq 0$ is the *atmospheric upwelling radiance* scattered at the sensor by the atmosphere (called *airlight* [42], equivalent to an additive term to be assessed by dark-object subtraction techniques: If, by definition of a dark object, $\rho = (1.2) = 0$, then the unknown variable L_a is equal to the measured TOARD value [43]). $E_d(n, \lambda) \geq 0$ is called *diffuse irradiance at the surface* [40], *ambient light*, or *indirect illumination* [44] it contains no information on the surface properties of the pixel and comprises two components.

1) In nonflat terrain areas, light is reflected from other objects (e.g., adjacent slopes in rugged terrain) before being reflected from the pixel under consideration. This first component is called *reflected terrain radiance* and is null in flat terrain [44].
2) In both flat and rugged terrain, radiation is reflected from the neighborhood of the pixel under consideration, and next, it is scattered by the atmosphere into the viewing direction. This second component is called *skylight* [42] or *adjacency radiance* [44].

Overall, $E_d(\lambda)$ changes with wavelength and can provide a relevant contribution to incident radiance [40], [43]. $\tau_{\mathrm{uw}}(\lambda) \in [0, 1]$ and $\tau_{\mathrm{dw}}(\lambda) \in [0, 1]$ are the *path atmospheric transmittances of the upwelling* (ground-surface–sensor path) and *downwelling* (Sun–ground-surface path) *flows*, respectively. $ESUN(\lambda)$ is the mean solar exoatmospheric (TOA, planetary) irradiance found in literature [41] (e.g., in the SPOT metadata DIMAP file format, parameter $ESUN(\lambda)$ is identified as "⟨SOLAR_IRRADIANCE_VALUE⟩"), $\theta_z \in [0, 90^\circ]$ is the Sun's zenith angle in degrees, typically provided in the image metadata file or computed from the data acquisition time t and per scene or pixel-based lat–long coordinates, and the term $[ESUN(\lambda)\cos(\theta_z)]$ is called *sunlight* [42] or *direct illumination* [44] and represents the only radiation component reflected from the pixel under consideration that contains "pure" information on the surface properties of the pixel.

In (1.2), atmospheric effects are modeled by atmospheric parameters $\tau_{\mathrm{uw}}(\lambda) \in [0, 1]$, $\tau_{\mathrm{dw}}(\lambda) \in [0, 1]$, and $L_a(\lambda) \geq 0$. To retrieve these atmospheric parameters, ancillary data (summary statistics), rarely available in practice, should be collected at several locations within the RS image footprint at the time of RS image acquisition. This means that the problem of atmospheric correction is typically ill or poorly posed. Consequently, it is very difficult to solve and requires user's supervision to make it better posed [12]. In practice, these authors have observed that RS images radiometrically calibrated into ρ values by several EU institutions mentioned hereafter in this paper are affected by spectral distortion causing scene-derived surface-reflectance spectra to disagree with reference surface-reflectance signatures found in existing literature (e.g., refer to [80, p. 273]) or in public domain spectral libraries such as the U.S. Geological Survey (USGS) mineral and vegetation spectral libraries, the Johns Hopkins University spectral library, and the Jet Propulsion Laboratory mineral spectral library [12], [73].

A reduction in interscene variability across time, space, and sensors can be achieved by a simplification of (1.2) into dimensionless TOARF values belonging to the range [0, 1]. Starting from (1.2), TOARF values are computed as a function of the electromagnetic wavelength for spectral band $b = 1, \ldots, Bnd$, by considering the following: 1) atmospheric effects negligible, such as for relatively "clear" scenes where $\tau_{\mathrm{uw}}(\lambda) \approx 1$, $\tau_{\mathrm{dw}}(\lambda) \approx 1$, and $L_a(\lambda) \approx 0$ [40], [43], and 2) flat and nonflat neighboring terrain effects negligible, i.e., $E_d(\lambda) \approx 0$ [40]. Thus, (1.2) becomes

$$TOARF(n, b, t, lat, long) = \frac{\pi \cdot d(t)^2 \cdot TOARD(n, b)}{ESUN(b) \cdot \cos\left(\theta_z(t, lat, long)\right)} \in [0, 1], \quad n = 1, \ldots, N;\ b = 1, \ldots, Bnd. \tag{1.3}$$

Although often overlooked by RS scientists and practitioners, it is well known in existing literature that the radiometric calibration of DNs into $TOARF = (1.3)$ values features several advantages over radiometric calibration into $TOARD = (1.1)$ values.

1) The former is recommended before calculating various vegetation indexes (VIs) [45]. In fact, while the relationships between the leaf area index (LAI) and a great variety of well-known VIs calculated from TOARD values are nonlinear, the relationships between LAI and the same vegetation indexes calculated from TOARF are, in several cases, reasonably linear.
2) By accounting for seasonal and latitudinal differences in solar illumination, the former guarantees better interimage comparability/interpretation (classification and mapping) across time, space, and sensors [46], [47], which is in line with the goals of EO data harmonization and interoperability required by the GEOSS and GMES programs.
3) The former is more consistent with the scenario of low- and high-level image-processing capabilities to be developed onboard future intelligent fourth-generation EO satellites (FIEOSs) [48], [49]. The development of FIEOSs, where onboard integration of sensors, data processors, and communication systems is pursued, should become a major scientific challenge to the RS community within the next ten years [48].

It is noteworthy that, when the diffuse irradiance at the surface is omitted, i.e., $E_d(\lambda) \approx 0$, then $\rho|_{Ed(\lambda)\approx 0} = (1.2)|_{Ed(\lambda)\approx 0} = f_1(TOARD)|_{Ed(\lambda)\approx 0}$ can be expressed as $\rho|_{Ed(\lambda)\approx 0} = f_2(TOARF)$ as follows:

$$\begin{aligned}\rho(n,\lambda,t,lat,long)\big|_{E_d(\lambda)=0} \in [0,1] \\ = TOARF(n,b,t,lat,long)\cdot\frac{1}{\tau_{\mathrm{uw}}(\lambda)\cdot\tau_{\mathrm{dw}}(\lambda)} \\ - \frac{\pi\cdot d(t)^2}{ESUN(\lambda)\cdot\cos\left(\theta_z(t,lat,long)\right)}\cdot\frac{L_a(\lambda)}{\tau_{\mathrm{uw}}(\lambda)\cdot\tau_{\mathrm{dw}}(\lambda)} \\ = (1.3)\cdot AtmphEffct_1(\lambda) \\ - \frac{\pi\cdot d(t)^2}{ESUN(\lambda)\cdot\cos\left(\theta_z(t,lat,long)\right)}\cdot AtmphEffct_2(\lambda), \\ n=1,\ldots,N;\ b=1,\ldots,Bnd \qquad (1.4)\end{aligned}$$

where $TOARF(n,b,t,lat,long) = (1.3) \in [0,1]$, $AtmsphEffct_1(\lambda) = \{1/[\tau_{\mathrm{uw}}(\lambda)\cdot\tau_{\mathrm{dw}}(\lambda)]\} \geq 1$, and $AtmsphEffct_2(\lambda) = \{L_a(\lambda)/[\tau_{\mathrm{uw}}(\lambda)\cdot\tau_{\mathrm{dw}}(\lambda)]\} \geq L_a(\lambda) \geq 0$. Vice versa

$$\begin{aligned}TOARF(n,b,t,lat,long)\big|_{E_d(\lambda)=0} \in [0,1] \\ = \rho(n,\lambda,t,lat,long)\big|_{E_d(\lambda)=0}\cdot[\tau_{\mathrm{uw}}(\lambda)\cdot\tau_{\mathrm{dw}}(\lambda)] \\ + \frac{\pi\cdot d(t)^2}{ESUN(\lambda)\cdot\cos\left(\theta_z(t,lat,long)\right)}\cdot L_a(\lambda) \\ = \frac{(1.2)\big|_{E_d(\lambda)=0}}{AtmphEffct_1(\lambda)} \\ + \frac{\pi\cdot d(t)^2}{ESUN(\lambda)\cdot\cos\left(\theta_z(t,lat,long)\right)}\cdot\frac{AtmphEffct_2(\lambda)}{AtmphEffct_1(\lambda)}, \\ n=1,\ldots,N;\ b=1,\ldots,Bnd. \qquad (1.5)\end{aligned}$$

Equation (1.4) shows that, if flat and nonflat neighboring terrain effects are negligible, i.e., $E_d(\lambda) \approx 0$, then the following are true.

1) For a clear sky condition, when $\tau_{\mathrm{uw}}(\lambda) \approx 1$, $\tau_{\mathrm{dw}}(\lambda) \approx 1$, and $\mathrm{L}_a(\lambda) \approx 0$ [40], [43], $AtmsphEffct_1(\lambda) \approx 1$ and $AtmsphEffct_2(\lambda) \approx 0$; thus, $\rho = (1.2) \approx (1.4) \approx$ TOARF $= (1.3) \approx (1.5)$, i.e., surface-reflectance ρ values can be computed from TOARF values when atmospheric effects are a) accounted for, i.e., scene-specific parameters $\tau_{\mathrm{uw}}(\lambda)$, $\tau_{\mathrm{dw}}(\lambda)$, and $L_a(\lambda)$ are retrieved from ancillary data or b) considered negligible. In other words, if $E_d(\lambda) \approx 0$, then $TOARF = (1.3) \approx (1.5) \supseteq \rho = (1.2) \approx (1.4)$. Intuitively, if $E_d(\lambda) \approx 0$, then $TOARF(\lambda) \approx \rho(\lambda) + AtmsphNoise(\lambda)$, where term $AtmsphNoise$ is zero for a clear sky condition. This (obvious) concept will be further recalled by the automatic LSRC system, described in Section II-D, and the integrated SRC system of systems, described in Section III, to be adopted as the automatic preliminary classification first stage of a two-stage stratified hierarchical RS-IUS instantiation (refer to Section II-C3c).
2) If $E_d(\lambda) = 0$, when atmospheric effects are omitted (ignored) independent of wavelength λ, i.e., $AtmsphEffct_1(\lambda) = 1$ and $AtmsphEffct_2(\lambda) = 0$ such that $\rho = (1.2) = (1.4) = TOARF = (1.3) = (1.5)$, numerical effects of the two simplified atmospheric terms $1 \leq AtmsphEffct_1(\lambda) = 1$ and $0 \leq L_{\mathrm{a}}(\lambda) \leq AtmsphEffct_2(\lambda) = 0$ tend to counterbalance each other, i.e., in (1.4), the first approximation causes an underestimation of the true ρ value, whereas the second approximation does the opposite. Across wavelengths, this property improves the effectiveness of TOARF as an estimator of the true ρ values.
3) When wavelength λ increases, TOARF provides a better approximation of ρ. It is well known that light scattering due to atmospheric conditions (haze, consisting of gas molecules and water droplets) and aerosols (consisting of liquid droplets and solid particles suspended in the atmosphere and generated by either natural or anthropogenic sources) is inversely proportional to the energy wavelength λ, i.e., shorter wavelengths of the spectrum are scattered more than the longer wavelengths [46]. Thus, a visible blue (B) channel is affected by scattering across all atmospheric conditions ranging from "very clear" (where scattering is proportional to a factor λ^{-4}) to "very hazy" (where scattering is proportional to a factor $\lambda^{-0.5}$) and cloudy (where complete scattering occurs, proportional to a factor λ^0) [43]. On the contrary, in the medium-infrared (MIR) wavelengths, the amount of atmospheric scattering is known to be "quite small except for very hazy atmospheres and can be considered negligible" [43, p. 476]. In these various combinations of atmospheric conditions with wavelengths ranging from very clear and clear atmosphere with visible wavelengths to any atmospheric condition occurring with the MIR portion of the electromagnetic spectrum unless it is very hazy, atmospheric effects can be omitted (ignored), i.e., $1 \leq AtmsphEffct_1(\lambda) = 1$ and $0 \leq L_{\mathrm{a}}(\lambda) \leq AtmsphEffct_2(\lambda) = 0$, such that, if $E_d(\lambda) = 0$, then $\rho = (1.2) = (1.4) = TOARF = (1.3) = (1.5)$.

C. RS-IUS Models and Implementations

This section reviews the model (architecture) design principles and inference (learning) mechanisms adopted by existing RS-IUSs. The goal of this survey section is to provide an LSRC and its original downscaled versions presented in Section III as the core of this paper with a suitable RS-IUS architecture eligible for use in operational satellite-based measurement systems such as those envisaged by the GEOSS and GMES programs.

1) Multiagent Hybrid RS-IUS Architecture: Multiagent hybrid RS-IUSs provide application-specific combinations of inductive and deductive inference mechanisms. A multiagent hybrid RS-IUS comprises the following modules (see Fig. 1).

1) (3-D) Scene domain knowledge (*world model*, refer to Section II-A) [19]. It is represented with semantic or concept nets defined as graphs, either directed or nonoriented, either cyclic or acyclic, consisting of nodes linked by edges. Nodes represent concepts, i.e., classes of objects in the world, while edges represent relations (e.g., PART-OF, A-KIND-OF, spatial relations [either topological, such as adjacency, inclusion, etc., or non-topological, such as metric distance and angle], and temporal transitions) between nodes [50], [97].

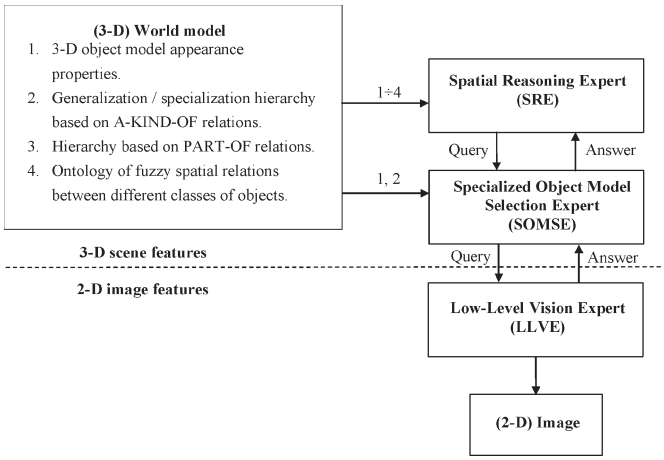

Fig. 1. Multiagent hybrid systems for RS image understanding (derived from [19, p. 36, Fig. 2.1]).

2) A Low-Level Vision Expert (LLVE) [19]. In general, an LLVE can be applied either imagewide or within a local image area specified by a Specialized Object Model Selection Expert [(SOMSE); see the following item] [19]. LLVE includes a battery of low-level subsymbolic (asemantic) general-purpose domain-independent inductive-learning (fine-to-coarse and bottom–up) driven-without-knowledge inherently ill-posed image-processing algorithms working at the signal level (data driven). This set of low-level image-processing algorithms may comprise edge-preserving noise filtering [51], [52], either intensity- or color-based region/edge detection [30], [53], texture-based region/edge detection, region growing [54], region extraction from not-close contours [55], etc. For simplicity's sake, all these image-processing operators are hereafter called *segmentation* [19]. As output, the image-segmentation first stage provides image features, namely, points and regions (segments, (2-D) objects, and blobs [32], [56], [57]) or, vice versa, region boundaries, i.e., edges, provided with no semantic meaning.
3) A high-level interpretation second stage employing a combination of top–down (model-driven) and bottom–up (data-driven) inference mechanisms to establish the correspondence between subsymbolic (2-D) image features extracted from the image domain and symbolic (3-D) object models stored in the world model to construct plausible structural (semantic) descriptions of the depicted scene (refer to Section II-A). The combination of top–down with bottom–up inference strategies [19] a) provides better conditions for an otherwise ill-posed driven-without-knowledge segmentation first stage and b) allows one to restrict intensive processing to a small portion of the image data, analogously to a focus of visual attention in preattentive biological vision [101]–[103]. The high-level processing second stage comprises [19] the following: 1) a Spatial Reasoning Expert (SRE) whose aim is to trigger the instantiation, within a candidate local area, of plausible generic (3-D) object models found in the available world model, e.g., a house, and 2) a SOMSE which uses domain-dependent knowledge about specific applications to perform the following: a) prune the search space of specialized (3-D) object models (e.g., rectangular house, L-shaped house, etc.) linked by A-KIND-OF relations to the generic target (3-D) object model (e.g., house) provided by SRE; b) transform the 3-D appearance properties of the specialized object model into a selected set of 2-D appearance properties based on the imaging sensor model; c) transform a target spatial relation in fuzzy terms (e.g., in front of) provided by SRE into a local area based on a trial-and-error heuristic search with no concrete theoretical basis; and d) provide a consistency examination between quantitative absolute image features collected by LLVE in a local area and the target 2-D appearance constraints. In other words, the 2-D appearance properties must be satisfied by image features extracted by LLVE from a local area. Since the image structure in a local area is very simple compared with that of the entire image, image feature extraction performed by an object model-driven and locational constrained LLVE can be very efficient and reliable compared with that performed by the same LLVE which is run imagewide at the first stage [19, p. 41].

Multiagent hybrid systems typically suffer from two main limitations.

1) In addition to the *intrinsic insufficiency* of image features, e.g., due to occlusion (refer to Section II-A), these systems are affected by the so-called *artificial insufficiency* caused by the inherent ill posedness of the image-segmentation problem. This means that, in RS common practice, any first-stage image-segmentation algorithm is simultaneously affected by both omission and commission segmentation errors. It is noteworthy that, although the inherent ill posedness of image segmentation is acknowledged by a reasonable portion of existing literature [19], [58]–[60], this is often forgotten by a large segment of the RS community where, literally, dozens of "novel" segmentation algorithms are published each year [9].
2) Semantic nets lack flexibility and scalability to cope with the users' changing needs, i.e., they are unsuitable for commercial RS image-processing software toolboxes and remain limited to scientific applications.

Examples of multiagent hybrid RS-IUSs found in existing literature are the blackboard model [61], SIGMA [19], ACRONYM [62], SPAM [63], AIDA [50], and ERNEST [64].

2) Two-Stage Segment-Based RS-IUS Architecture: Since the mid-1980s, increasing awareness of the serious drawbacks affecting ordinary top–down model-driven decision-tree classifiers developed by the symbolic artificial intelligence [65], namely, intrinsic lack of flexibility (i.e., rules do not adapt to change and the knowledge base may soon become obsolete) and scalability (i.e., rule-based systems are impractical for complex problems), urged RS scientists and practitioners to find adaptive solutions to their changing needs (also refer to Section II-C1). To date, in RS common practice and in commercial RS image-processing software toolboxes [11], a two-stage segment-based

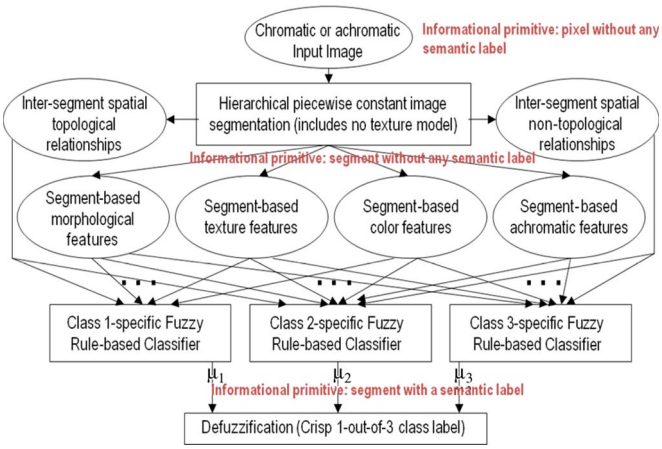

Fig. 2. Two-stage segment-based RS-IUS architecture adopted, for example, by the eCognition commercial software toolbox [11]. Preliminary image simplification is pursued by means of an (ill-posed hierarchical) image-segmentation approach which generates, as output, a segmented (discrete) map, either single-scale or multiscale. Worthy of note is that first-stage output subsymbolic informational primitives, namely, labeled segments (2-D objects and parcels), e.g., segment 1, segment 2, etc., are provided with no semantic meaning.

RS-IUS architecture (well known in existing literature as (2-D) object-based image analysis (OBIA) [60]) has recently gained remarkable popularity and is considered the state-of-the-art [66], e.g., in VHR image understanding where geometric attributes and spatial relationships are particularly important for the recognition of man-made objects, such as buildings, roads, and agricultural fields [19].

Unlike multiagent hybrid RS-IUSs, a two-stage segment-based RS-IUS comprises an inherently ill-posed driven-without-knowledge segmentation first stage in series with a segment-based classifier unable to interact with the first-stage segmentation to make it better posed. In particular, (see Fig. 2) the two stages are as follows.

1) The inherently ill-posed driven-without-knowledge segmentation first stage is as follows: a) affected by artificial insufficiency which causes the simultaneous presence of omission and commission segmentation errors (see Section II-C1) and b) relies on segmentation parameters to be user defined based on heuristics, i.e., it is difficult to use. To reduce the number of empirical segmentation parameters [98], commercial two-stage segment-based RS-IUSs employ a multiscale (hierarchical) iterative segmentation first stage [11]. As output, a hierarchical segmentation algorithm generates multiscale segmentation solutions in the hope that the target image will appear correctly segmented at some scale. Unfortunately, the quantitative multiscale assessment of segmentation quality indexes requires ground truth data at each scale that are impossible or impractical to obtain in RS common practice [67]. Therefore, the "best" segmentation map must be selected by the user on an *a posteriori* basis from the available set of multiscale segmentation solutions according to heuristic, subjective, and/or qualitative criteria analogous to those employed in the selection of prior segmentation parameters. To conclude, the exploitation of a hierarchical segmentation algorithm does not make the driven-without-knowledge segmentation first stage easier to use. In addition, hierarchical segmentation algorithms are computationally intensive and require large memory occupation.
2) A segment-based classification second stage can be implemented either top–down (model driven), such as a decision-tree classifier based entirely upon prior knowledge of the (3-D) world [11], or bottom–up (data driven), such as a supervised data learning classifier [29], [33], [68]. In practice, under the guise of "flexibility," two-stage segment-based RS-IUS software toolboxes provide RS experts and practitioners with overly complicated options to choose from based on heuristics, i.e., they are difficult to use [60]. In addition, the second-stage classifier is unable to interact with the inherently ill-posed driven-without-knowledge segmentation first stage to make it better posed (see Section II-C1). Finally, as input information primitives, the second stage classifier employs subsymbolic (2-D) segments exclusively. This is unnecessary and time consuming when pixel-based spectral properties are sufficient for classification purposes.

To date, the conceptual foundation of OBIA, i.e., the relationship between inherently ill-posed subsymbolic (2-D) image segments and symbolic (3-D) landscape objects, remains affected by a lack of general consensus and research [60].

3) Two-Stage Stratified Hierarchical RS-IUS Architecture: In recent years, Shackelford and Davis presented several implementations of an original two-stage RS-IUS architecture suitable for mapping VHR satellite images of urban areas [21], [25], [26]. Starting from the customary distinction between a model and the algorithm used to identify it [28], the family of Shackelford and Davis RS-IUS implementations constitutes an original subclass of the parent class of multiagent hybrid RS-IUSs (see Section II-C1). This subclass is identified as the two-stage stratified hierarchical RS-IUS architecture alternative to the traditional two-stage segment-based RS-IUS model (see Section II-C2).

a) Shackelford and Davis implementation: Suitable for mapping a 1-m-resolution panchromatic (PAN)-sharpened MS IKONOS image of urban areas, the Shackelford and Davis two-stage RS-IUS implementation comprises, in cascade (see Fig. 3), the following [21], [25], [26].

1) A pixel-based preliminary classifier implemented as a supervised pixel-based plug-in (i.e., nonadaptive noniterative) maximum likelihood (ML) classifier. It maps each pixel into a discrete and finite set of semantic labels. In place of ordinary land cover classes, these labels identify land-cover-class sets [25], [26], i.e., "combine" sets of primitive land cover classes. More specifically, each class set is a logical OR combination of primitive land cover classes affected by ML classification confusion due to a significant amount of spectral overlap. This is tantamount to saying that the ML classification confusion between different class sets is negligible, i.e., land-cover-class sets must be mutually exclusive. In other words, the first-stage pixel-based plug-in ML classifier implemented by Shackelford and

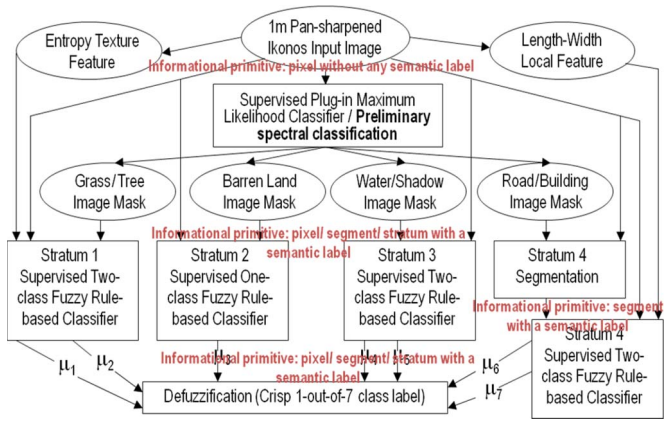

Fig. 3. Two-stage stratified hierarchical RS-IUS implementation proposed by Shackelford and Davis [21], [25], [26]. A preliminary spectral classification first stage provides, as output, symbolic informational primitives featuring three spatial types, namely, symbolic pixels in symbolic segments (2-D objects, parcels, as connected sets of labeled pixels featuring the same label) in symbolic strata (as image-wide sets of labeled pixels featuring the same label), all provided with a symbolic (semantic) meaning (e.g., vegetation) easy to understand by the application developer familiar with symbolic reasoning. In this work, the plug-in pixel-based ML classifier, adopted by Shackelford and Davis to instantiate the preliminary spectral classification first stage of a two-stage stratified hierarchical RS-IUS architecture [21], [25], [26], is replaced by a noniterative (one-pass) pixel-based fully automated decision-tree SRC system of systems (refer to Section III).

Davis is well posed. Given the structural content of urban scenes depicted in VHR spaceborne imagery, five class sets are identified (see Fig. 3): a) *either grass or tree*; b) *either road or building or impervious surface*; c) *either water or shadow*; d) *bare soil*; and e) *others* (outliers, e.g., clouds). In line with the Congalton requirements, this classification scheme is mutually exclusive and totally exhaustive [69, p. 12].

2) A battery of land-cover-class (3-D object model)-specific (knowledge-driven) hierarchical classifiers incorporating the "stratified" or "layered" approach which is typically adopted in decision trees [18], [21], [25], [26]. This battery consists of (see Fig. 3) the following: a) stratified context-sensitive (e.g., texture) feature-extraction modules and b) stratified land-cover-class-specific fuzzy-rule-based classification modules employing a convergence-of-evidence mechanism.

b) Advantages of the two-stage stratified hierarchical RS-IUS architecture: In comparison with the parent class of multiagent hybrid RS-IUSs (refer to Section II-C1), the subset class of two-stage stratified hierarchical RS-IUSs features one major advantage. While primitive (2-D) objects employed by the former are subsymbolic (asemantic) segments (e.g., segment 1, segment 2, etc.), the latter employs primitive (2-D) objects comprising symbolic pixels in symbolic segments in symbolic strata. In practice, by providing RS application developers and domain experts with semantic (symbolic) primitive (2-D) objects in the image domain, the two-stage stratified hierarchical RS-IUS architecture facilitates the instantiation of multiagent hybrid systems for RS image understanding.

In comparison with the two-stage segment-based RS-IUS architecture (refer to Section II-C2), the two-stage stratified hierarchical RS-IUS model features several potential advantages which are listed as follows.

1) A pixel-based preliminary classification first stage features several advantages over a first-stage driven-without-knowledge segmentation algorithm.
   a) The former is not affected by the well-known *uncertainty principle* according to which, for any contextual (neighborhood) property, we cannot simultaneously measure that property while obtaining accurate localization [67], [104]. In other words, by working at the sensor SR, the pixel-based preliminary classification first stage offers a capability of detecting small but genuine image details that is potentially superior (at least not inferior) to that of any context-sensitive inherently ill-posed segmentation algorithm. In addition, by working at the sensor resolution, the former mapping approach is SR independent.
   b) As output, a pixel-based preliminary classifier identifies mutually exclusive class sets, hereafter called *spectral-based semiconcepts* [105] that, by definition, are affected by no spectral overlap. This is tantamount to saying that *a pixel-based preliminary classifier is well posed and capable of removing any source of artificial insufficiency* (uncertainty and unreliability) of subsymbolic image features traditionally introduced by a first-stage ill-posed driven-without-knowledge segmentation algorithm (refer to Section II-C1). *A spectral-based semiconcept is a semantic conjecture based solely on the per-pixel (noncontextual) color (spectral, i.e., chromatic and achromatic) properties*. For example, if the "color" (spectral signature) of a pixel is, for example, green/brown/blue/white in the visible electromagnetic spectrum, then that pixel is likely to belong to a spectral-based semiconcept, equivalent to a color-based semantic conjecture, called *vegetation/bare soil or built-up/water/cloud or snow*, respectively, whose information granularity is equal or coarser than that of its primitive land cover classes (concepts in the (3-D) world) such as, for example, *forest* or *grassland* both mapped onto spectral category *vegetation*. In practice, *spectral-based semiconcepts are suitable for filling in the well-known information gap (intrinsic insufficiency) between concepts in the (3-D) scene and subsymbolic features in the (2-D) image* (refer to Section II-A). Since *spectral-based semiconcepts are affected by no spectral overlap, they are reliable (robust) and eligible for splitting into their primitive land cover classes at a further hierarchical RS data-processing level when additional sources of contextual evidence (e.g., textural, morphological, etc.) are taken into consideration*.
   c) While driven-without-knowledge segmentation provides ill-posed image segments as subsymbolic primitive (2-D) objects, a pixel-based preliminary classification first stage generates as output symbolic primitive (2-D) objects comprising symbolic pixels in symbolic segments in symbolic strata. These three

spatial types are not alternative, but they coexist and can be selected according to the needs of the second-stage battery of application-specific satellite-based measurement systems (refer to the following).

2) In series with the preliminary image classification first stage, a battery of second-stage stratified class-specific hierarchical classification modules enforces a well-known divide-and-conquer problem-solving approach traditionally employed by decision-tree classifiers [18]. The idea of stratification is well known in statistics. For example, in stratified sampling, the sampling frame is divided into nonoverlapping groups or strata, e.g., geographical areas. A sample is taken from each stratum, and when this sample is a simple random sample, it is referred to as stratified random sampling. The advantage is that "*stratification will always achieve greater precision provided that the strata have been chosen so that members of the same stratum are as similar as possible in respect to the characteristic of interest*" [70]. A possible disadvantage is that identifying appropriate strata may be difficult. The second-stage battery of stratified class-specific hierarchical classification modules consists of the following (see Fig. 3).
   a) Stratified class-specific context-sensitive (e.g., texture, morphological, and geometric) feature-extraction modules. For example, the stratified or layered approach is adopted to make an inherently ill-posed segmentation algorithm better posed (locational constrained) [19]. In particular, a second-stage class-specific stratified segmentation algorithm can be employed when a target land cover class is characterized by salient geometric (morphological and shape) properties to be computed segment based. This is typically the case of man-made objects, such as buildings, roads, and agricultural fields, whose geometric attributes are particularly important for their recognition (see Fig. 3).
   b) Stratified class-specific fuzzy-rule-based classification modules employing constructive reasoning [19]. In practice, constructive reasoning is pursued through evidence accumulation (convergence of evidence) by means of fuzzy membership functions (e.g., elongatedness is high) and fuzzy operators (fuzzy-AND, fuzzy-OR, etc.) [25], [26]. It is noteworthy that if–then rules combining symbolic and subsymbolic sources of evidence can be, first, easily modeled by a human domain expert who is naturally acquainted with symbolic reasoning and, second, implemented seamlessly in a two-stage stratified hierarchical RS-IUS architecture. For example, a *ship* detection rule can be written in natural language by a human expert based on the convergence of context-insensitive preliminary automatically detected spectral-based symbolic strata (see Section II-D) with geometric, morphological, and spatial properties, either topological (e.g., adjacency) or nontopological (e.g., spatial distance), as follows: A (2-D) image segment detected by a well-posed segmentation algorithm in the preliminary classification map domain whose elongatedness is (fuzzy) high, whose length is between 3 and 300 m (e.g., equivalent to 3–300 pixels in a 1-m-resolution image), whose spectral signature belongs to the *bare soil or built-up* preliminary spectral category (refer to Section II-D), and which is adjacent to a large *water or shadow* body or in the vicinity of a large *water or shadow* body is likely to belong to the (3-D) object class *ship* (refer to Fig. 15 in Part II of this paper). It is noteworthy that, in this example, spectral categories *bare soil or built-up* and *water or shadow* are required as preliminary semantic types whose levels of specialization are inferior to that of the (3-D) object class *ship* in a hierarchical decision-tree structure.

3) In a two-stage stratified hierarchical RS-IUS architecture, the world model is twofold.
   a) A first-stage world model stored in the pixel-based preliminary classifier. It consists of spectral-based semiconcepts described in terms of the terminology defined in the (3-D) world (e.g., *either water or shadow*).
   b) A second-stage world model consisting of semantic nets whose nodes [(3-D) object models] incorporate the stratified or layered approach. This means that, in addition to the 3-D appearance properties (e.g., the length of a ship is between 3 and 300 m), an object model comprises, among its attributes, a list of color-based semiconcepts equivalent to a model-specific locational constraint based on color properties (focus of attention by stratification, e.g., the spectral signature of a ship belongs to the *either bare soil or built-up* spectral category automatically detected in the preliminary classification first stage).

These considerations imply that the degree of prior knowledge required to complement the intrinsic insufficiency of (2-D) image features (see Section II-A) embedded in the two-stage stratified hierarchical RS-IUS model is superior to that adopted by the two-stage segment-based RS-IUS architecture (see Section II-C2). As a consequence, the former RS-IUS architecture is eligible for finding a better solution to the ill-posed image-understanding problem than the latter.

c) Enhanced two-stage stratified hierarchical RS-IUS implementation: The main drawback of the two-stage stratified hierarchical RS-IUS implementation proposed by Shackelford and Davis is its request for supervised training data at every hierarchical stage [21], [25], [26]. Unfortunately, the cost, quality, and availability of adequate training labeled (reference) samples are the most limiting factor on the applicability of scene-by-scene inductive supervised data learning algorithms (e.g., artificial neural networks [29], [33]) to RS data understanding problems whose input data set can be acquired across time, space, and sensors (refer to Section I) [71].

To reduce to zero the need for supervised training data of the plug-in ML classifier implemented by Shackelford and Davis as the preliminary spectral classification first stage, the fully automated LSRC system can be adopted instead (refer to Section II-D).

D. LSRC

Recently proposed to the RS community, LSRC is an automatic top–down per-pixel spectral prior-knowledge-based decision-tree classifier requiring, as input, a radiometrically calibrated seven-band Landsat-like image [20], [27], [72]. The degree of novelty of LSRC is fivefold.

1) *LSRC requires neither user-defined parameters nor reference data samples to map a radiometrically calibrated MS imagery acquired across time, space, and sensors*, such as the Landsat-4/-5 Thematic Mapper (TM), the Landsat-7 Enhanced TM (ETM)+, the ASTER, and the Moderate Resolution Imaging Spectroradiometer (MODIS). Therefore, LSRC is termed "*fully automated*" [106]. To the best of our knowledge, no multisource multiresolution fully automated optical image mapping system alternative to LSRC exists in RS literature.
2) LSRC is a pixel-based one-pass (noniterative) decision-tree classifier that is not adaptive to data, i.e., LSRC is model based (refer to Section I) where (3-D) object models belonging to the (3-D) world model (refer to Section II-A) rely upon prior spectral knowledge exclusively. The LSRC prior spectral knowledge base consists of decision rules generated from endmember collection spectra extracted from a wide variety of real-world MS satellite images that are radiometrically calibrated into $TOARF = (1.3)$ values rather than surface-reflectance $\rho = (1.2)$ values adopted by competing approaches in the domain of RS spectral-pattern (shape) matching [73]–[75], such as the Environment for Visualizing Images (ENVI), licensed by ITT Industries, Inc. [73], and ATCOR3 [12]. It is noteworthy that, when indirect illumination is negligible, i.e., if $E_d(\lambda) \approx 0$, then $TOARF = (1.3) \supseteq \rho = (1.4)$, the latter being an ideal case of the former when atmospheric effects are considered negligible (refer to Section II-A). Therefore, the reference dictionary of endmember spectra in TOARF values employed by LSRC adopts well-known ground-measured or library surface-reflectance spectra as a specific (ideal and atmospheric-noise-free) case [12], [73]. This is tantamount to saying that, in agreement with the QA4EO initiative (see Section I), the only requirement of the operational automatic LSRC is to employ, as input, a well-behaved *MS image radiometrically calibrated into either* $TOARF = (1.3)$ *or* $\rho = (1.2)$ *values*. As a consequence, LSRC may benefit from, but requires no inherently ill-posed atmospheric-correction preprocessing stage (refer to Section II-B). In other words, LSRC considers atmospheric correction an optional MS image preprocessing step unlike competing classification approaches employing surface-reflectance spectra, such as ATCOR3 [12], for which the solution of the ill-posed atmospheric-correction problem becomes mandatory. At best [when it introduces no spectral distortion (refer to Section II-B)], a mandatory atmospheric-correction stage decreases the overall operational performance measurement of an RS data product generation and delivery chain, due to a decrease in the degree of automation, an increase of costs required to gather ancillary data, and an overall increase of timeliness (refer to Section I).
3) In LSRC, for each family of reference spectral signatures in TOARF values (e.g., vegetation), a human spectral analyst employs an original two-step spectral signature modeling procedure [27]. In particular, the spectral (pattern) shape of the target family of reference signatures is modeled in terms of, first, interband relations, e.g., band $1 \geq$ band 2 with a 10% tolerance, i.e., band $1 \geq (0.9 * \text{band } 2)$ and, second, per-band intensity/range of variation, e.g., band 1 is either high or medium. Worthy of note is that, unlike LSRC, ordinary spectral-pattern (shape) matching classifiers, such as the spectral angle mapper (SAM) which is well known for its relative insensitiveness to illumination and albedo effects [73]–[75], ignore intensities of input data vectors. The aforementioned LSRC two-step spectral signature modeling strategy generates, as output, a two-layer hierarchy of fuzzy production rules (if–then rules) per spectral category equivalent to a decision-making mechanism based on accumulation of evidence (convergence of evidence) [27]. In LSRC, accumulation of evidence decreases the total amount of effort spent in the search among alternative hypotheses of plausible spectral-based semiconcepts and increases the reliability of the constructive image understanding procedure.
4) LSRC automatically detects, as output, spectral-based semiconcepts which, by definition, are affected by no spectral overlap (refer to Section II-C3b). *While (3-D) land cover classes (e.g., deciduous forest) are provided with a superior semantic meaning, but are difficult to detect automatically, (2-D) spectral-based semiconcepts (e.g., vegetation), which are provided with an inferior semantic meaning, are detected automatically by LSRC* [27]. For example, LSRC maps every pixel-based seven-band Landsat-like data vector onto a discrete and finite set of 46 spectral categories belonging to six *parent* spectral categories (supercategories) which are listed as follows (according to their order of detection): a) *cloud*; b) *either snow or ice*; c) *either water or shadow*; d) *vegetation*; e) *either bare soil or built-up*; and f) *outliers* [27]. It is worthy of note that each aforementioned spectral category is named after the set of (3-D) land cover classes providing the reference ensemble of spectral signatures (refer to point 2) earlier in this paper) associated with that spectral (color) behavior. For example, let us consider the realistic case where, at the Landsat sensor-specific spectral and spatial resolutions, LSRC assigns a spectral-based semiconcept *either bare soil or built-up* to unlabeled pixels depicting an instance of the (3-D) object class (concept) *ship* (refer to Section II-C3b of this paper and Fig. 15(a) in Part II of this paper). By assigning a per-pixel MS data vector belonging to an instance of the (3-D) class *ship* with a (2-D) color-based semiconcept *either water or shadow*, LSRC means that an input unlabeled data vector looks like, i.e., shares the same MS properties as, the family of reference spectral signatures generated from the land-cover-class set *either water or shadow*. By no means should this mapping occurrence

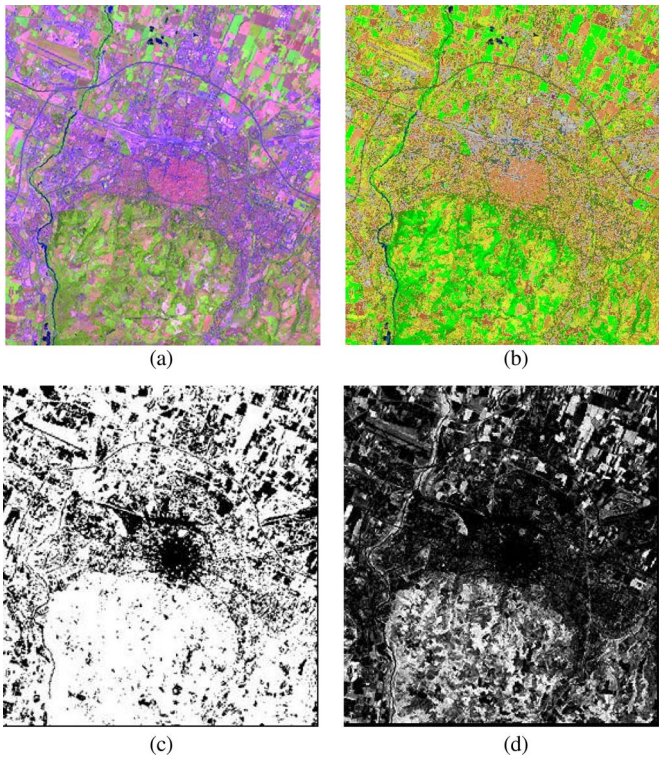

Fig. 4. (a) Zoomed image of the city of Bologna, Italy, extracted from a Landsat 7 ETM+ image (path 192, row 029, acquisition date: June 20, 2000), radiometrically calibrated into TOARF values and shown in false colors [(R) band TM5, (G) band TM4, (B) band TM1]. (b) Output map, shown in pseudocolors, generated by LSRC from the radiometrically calibrated image shown in (a). Water and shadow areas are in blue, clouds are in white, snow and ice are in light blue, vegetation types are in different shades of green, rangeland types are in different shades of light green, and barren land types are in different shades of brown and gray. (c) Binary mask showing, in white, spectral categories found in (b) related to vegetated land covers. (d) "Intelligent" greenness index generated from (a), masked by (c), whose value is exactly zero for nonvegetated surface types.

be considered a classification error where an instance of the (3-D) object class (concept) *ship* is (mis)labeled by LSRC as belonging to the OR combination of (3-D) object classes (concepts) *bare soil* and *built-up*.

5) In terms of operational performance, LSRC scores high. According to [27], it can be considered as follows: a) fully automated (see earlier discussion); b) accurate (see Fig. 4); c) near real time (e.g., it requires approximately 5 min to process a Landsat scene on a desktop computer provided with a dual-core Pentium processor); d) robust to changes in the input image acquired across time, space, and sensors; e) capable of providing a preliminary classification map whose semantic granularity is much finer than that provided by the ML first stage of the Shackelford and Davis RS-IUS implementations (see Section II-C3a); and f) not affected by the well-known salt-and-pepper classification noise effect which traditionally affects ordinary pixel-based classifiers, i.e., LSRC is successful in modeling the within-stratum variance. These functional attributes make LSRC eligible for use as the preliminary pixel-based classification first stage in a two-stage stratified hierarchical RS-IUS architecture (see Section II-C3c). This means that, *in a two-stage stratified hierarchical RS-IUS instantiation* (see Fig. 3) *employing LSRC as its pixel-based preliminary classification first stage, second-stage traditional algorithms capable of learning from either unlabeled or labeled data*, such as unlabeled data clustering and image-segmentation algorithms, *which incorporate the stratified or layered approach are expected to perform better than or the same as their traditional nonstratified counterparts.* This is tantamount to saying that an *operational automatic LSRC system is preliminary and by no means alternative to traditional algorithms capable of learning from either unlabeled or labeled data* (e.g., the spectral-pattern matching classifier SAM [73]–[75]), *which can be enhanced by incorporating the stratified or layered approach*.

To conclude, by mapping an MS image into a discrete and finite set of color-based semiconcepts [see point 4) earlier] at a degree of user's supervision equaling zero [see point 1) earlier] and in near real time [see point 5) earlier], LSRC reverses the meaning of a well-known observation, namely, one image (featuring a high degree of nonsymbolic pictorial information) is worth a million words (which, instead, are useful in symbolic reasoning). The high degree of novelty of LSRC proves that, in computer vision, one (2-D) symbolic information primitive (semiconcept) in the image domain is worth a thousand subsymbolic image features, namely, points and regions or region boundaries, i.e., edges.

Among existing commercial software toolboxes, the popular ATCOR3 classifier [12], which exploits a traditional endmember collection spectra in surface-reflectance ρ values, can be considered a realistic semiautomatic alternative to the operational automatic LSRC system. In ATCOR3, the pixel-based spectral classification of the reflectance cube (SPECL) is based upon template spectra at the Landsat TM reference wavelengths (i.e., 0.48, 0.56, 0.66, 0.83, 1.6, and 2.2 μm). Families of template spectra represent land cover classes such as bright sand, sand/bare soil, asphalt/man-made, green vegetation, yellow vegetation, dark vegetation, and water. If the pixel-based spectral reflectance signature agrees within a 10% margin at the reference wavelengths with one of the class template spectra, then that pixel is labeled with that class index; otherwise, it is assigned to class unknown. It is noteworthy that, unlike LSRC, SPECL is input with a spaceborne MS image preprocessed as follows.

1) The raw DNs are transformed into TOARD values based on the radiometric calibration metafile.
2) TOARD values are transformed into surface-reflectance values after an empirical atmospheric-correction stage where the user selects a combination of the following:
   a) an atmosphere (visibility in kilometers or, vice versa, optical depth, e.g., a summer atmosphere);
   b) an aerosol (e.g., maritime/rural/urban/desert aerosol);
   c) a water vapor column (in centimeters, e.g., tropical conditions/midlatitude summer/dry summer, spring, or fall/dry desert or winter).
3) An empirical bidirectional reflectance distribution function effect correction stage, equivalent to an empirical

TABLE I
SPECTRAL RESOLUTION OF THE LANDSAT-5 TM AND LANDSAT-7 ETM+ SENSORS IN COMPARISON WITH SPECTRAL RESOLUTIONS OF THE ASTER TERRA AND MODIS SATELLITE SENSORS

Landsat 5 TM and 7 ETM+ (30 m SR)		ASTER Terra (15-30 m SR)		MODIS (250, 500, 1000 m SR)	
Band	Spectral region (μm)	Band	Spectral region (μm)	Band	Spectral region (μm)
1 (B)	0.45-0.52	-	-	(3+10) OR 3	[(0.459 – 0.479) + (0.483 – 0.493)] OR (0.459 – 0.479)
2 (G)	0.52-0.60	1	0.52-0.60	(11+4) OR 4	[(0.526 – 0.536) + (0.545 – 0.565)] OR (0.545 – 0.565)
3 (R)	0.63-0.69	2	0.63-0.69	(1+14) OR 1	[(0.620 – 0.670) + (0.673 – 0.683)] OR (0.620 – 0.670)
4 (NIR)	0.76-0.90	3	0.76-0.86	(15+2+17) OR (15+16+17) OR 2	[(0.743 – 0.753) + (0.841 – 0.876) + (0.890 – 0.920)] OR [(0.743 – 0.753) + (0.862 – 0.877) + (0.890 – 0.920)] OR (0.841 – 0.876)
5 (MIR1)	1.55-1.75	4	1.600-1.700	6	1.628 – 1.652
7 (MIR2)	2.08-2.35	(5 + 6 + 7 + 8)	[(2.145-2.185) + (2.185-2.225) + (2.235-2.285) + (2.295-2.365)]	7	2.105 – 2.155
6 (TIR)	10.4-12.5	(13+14)	[(10.25-10.95) + (10.95-11.65)]	(31+32)	[(10.780 - 11.280) + (11.770 - 12.270)]

nonstratified topographic correction [20], where a pixel-based illumination angle is computed as a function of the following: a) a digital elevation model and b) the solar zenith angle.

To summarize, LSRC totally differs from ATCOR3 in the following: 1) the physical unit of endmember collection spectra (respectively, TOARF versus ρ values); 2) the semiautomatic ill-posed atmospheric-correction preprocessing stage (optional for the former and compulsory for the latter); and 3) the classification stage (consisting of a two-stage decision-tree classifier in the former [refer to point 3) in the earlier discussion] and a metrological measure of vector pair matching in the latter).

III. DOWNSCALED LSRC SYSTEM IMPLEMENTATIONS

When both past and ongoing EO satellite optical missions are taken into consideration, existing literature considers the Landsat-5 TM and Landsat-7 ETM+ combination of spatial and spectral resolutions fine enough for addressing most of the environmental and ecological problems [74]. A significant portion of the RS community considers the Landsat data of such a tremendous scientific utility as to urgently require a follow-on mission to Landsat-7[5] [2, p. 451]. In agreement with this portion of the RS community, both LSRC and ATCOR3 adopt the Landsat spectral resolution as a community-agreed reference standard (refer to Section II-D) [27].

To be input with RS images acquired by spaceborne and airborne data sources (identified hereafter as "slave" sensors) different from the Landsat sensor series (identified as the reference standard or "master" sensor), it is possible to perform the following.

1) Upscale the LSRC rule set to MS images, radiometrically calibrated into TOARF values, whose spectral resolution is superior to Landsat's, e.g., MODIS (250-, 500-, and 1000-m SR), ASTER (15–30-m SR), and aerial hyperspectral sensors such as the Specim AISA DUAL, the Itres SASI 600 and CASI 1500, and the Galileo Avionica SIM-GA (refer to Table I).
2) Apply LSRC as it is to MS images, radiometrically calibrated into TOARF values, featuring the Landsat spectral resolution, e.g., CBERS-2B (20-m SR; unfortunately, CBERS-2B is affected by serious radiometric calibration problems).
3) Downscale the LSRC rule set to MS images, radiometrically calibrated into TOARF values, whose spectral resolution is inferior to Landsat's, i.e., when one or more Landsat spectral bands are not present [e.g., SPOT-4/-5 (refer to Table II)].

In practice, to find a correspondence between the master and the slave spectral response sensitivity curve, each individual Landsat band must be mapped onto bands of the slave sensor, if any. Two mapping cases occur.

1) Across the target Landsat spectral bandwidth, the spectral response of the slave sensor is equal to zero. In this case, the target Landsat band is removed from the downscaled LSRC rule set.

[5]Launched in April 1999, Landsat-7 ETM+ continues to acquire data globally. The Scan Line Corrector failure in April 2003 has affected ground coverage and the switch to Bumper Mode operations in April 2007 has degraded the internal geometry accuracy of the data, but the radiometry has been unaffected. Launched in March 1984, Landsat-5 TM continues to acquire global data. A technical failure of one of the transmitters in 1987 means that only data acquired within an acquisition circle of a ground station can be downlinked. The TM scanner was switched to Bumper Mode operations in April 2002 which has degraded the internal geometry accuracy of the data, but the radiometry has been unaffected [76]. A major system failure of the Landsat-5 TM mission is considered very likely to occur within the year 2010 [107].

TABLE II
SPECTRAL RESOLUTION OF THE LANDSAT-5 TM AND LANDSAT-7 ETM+ SATELLITE SENSORS IN COMPARISON WITH THE SPECTRAL RESOLUTIONS OF THE SPOT-4 HRVIR, SPOT-5 HRG, SPOT-4/-5 VMI, ENVISAT AATSR, NOAA AVHRR, AND MSG SATELLITE SENSORS

Landsat 5 TM and 7 ETM+ (30 m SR)		SPOT-4 HRVIR (20 m SR), SPOT-5 HRG (10 m SR) and SPOT-4/-5 VMI (1.1 km SR)		ENVISAT AATSR (1 km SR)		NOAA AVHRR (1.1 km SR)		MSG (3 km SR)	
Band	Spectral region (μm)	Band	Spectral region (μm)	Band	Spectral region (μm)	Band	Spectral region (μm)	Band	Spectral region (μm)
1 (B)	0.45 - 0.52	1 (VMI)	0.43 -0.47	-	-	-	-	-	-
2 (G)	0.52-0.60	1 (HRVIR, HRG)	0.50-0.59	1	0.545-0.565	-	-	-	-
3 (R)	0.63-0.69	2	0.61-0.68	2	0.649-0.669	1	0.58-0.68	1	0.6
4 (NIR)	0.76-0.90	3	0.78-0.89	3	0.855-0.875	2	0.725-1.10	2	0.8
5 (MIR1)	1.55-1.75	4	1.58-1.75	4	1.46-1.76	3(A)	1.58-1.64	3	1.6
7 (MIR2)	2.08-2.35	-	-	-	-	-	-	-	-
6 (TIR)	10.4-12.5	-	-	6 OR (6 + 7)	(10.35-11.35) OR [(10.35-11.35) + (11.50-12.50)]	4+5	[(10.30-11.30) + (11.50-12.50)]	8 OR 9	10.8 OR 12.0

2) The Landsat band-specific spectral response sensitivity curve can be approximated by a linear combination of the slave band-specific spectral response sensitivity curves (e.g., refer to Table I). Since a spectral response sensitivity curve determines the amount of at-sensor radiance $TOARD = (1.1)$ and, as a consequence, at-sensor reflectance $TOARF = (1.3)$, the approximation of the Landsat band-specific sensitivity curve introduces an approximation of the reference TOARF values. To be considered negligible by the downscaled LSRC version, this approximation must fall below the band-specific range of spectral change assigned by LSRC to each spectral category (refer to Section II-D). If this approximation is within tolerance, then 1) the selected linear combination of bands in the slave image is performed in the calibration preprocessing phase, i.e., before running the downscaled LSRC version, and 2) the target Landsat band is maintained in the downscaled LSRC rule set.

In comparison with LSRC, capable of detecting 46 spectral categories [27], a downscaled LSRC version affected by the loss of one or more Landsat bands may be affected by the following: 1) a loss of spectral indexes [e.g., VI, bare soil index, etc. (refer to Section V)] and their fuzzy sets (e.g., VI is high, medium, or low) that cannot be computed (refer to Table III in [27]); 2) a loss of so-called spectral rules [e.g., band $1 \geq (0.9 * \text{band } 2)$] that cannot be computed or coincided (refer to Table IV in [27]); and 3) a loss of spectral categories [e.g., *either snow or ice* (refer to Section II-D)] that cannot be computed or coincided (refer to Table V in [27]).

Let us identify the seven Landsat-like bands employed as input by LSRC as follows: ETM1 for visible B (0.45–0.52 μm), ETM2 for visible green [(G); 0.52–0.60 μm], ETM3 for visible red [(R); 0.63–0.69 μm], ETM4 for near IR [(NIR); 0.76–0.90 μm], ETM5 for MIR1 (1.55–1.75 μm), ETM7 for MIR2 (2.08–2.35 μm), and ETM6 for thermal IR [(TIR); 10.4–12.5 μm] (refer to Table I). Starting from [27], where enough information is provided to the reader for the seven-band LSRC implementation to be reproduced, the five downscaled versions of LSRC suitable for employing, as input, an MS image, radiometrically calibrated into TOARF values, acquired by almost any of the existing or future planned satellite optical imaging sensors (for example, refer to Tables I and II) whose spectral resolution overlaps with, but is inferior to Landsat's, can be implemented as follows.

1) Four-band SPOT-like SRC (SSRC). The four spectral channels are G, R, NIR, and MIR1. The removed Landsat bands are B, MIR2, and TIR.
   a) The target satellite sensors are the SPOT-4 High Resolution Visible and IR (HRVIR) (MS: 20-m SR, PAN: 10-m SR), SPOT-5 High Resolution Geometric (HRG) (MS: 10-m SR, PAN: 2.5 ÷ 5 m SR), SPOT-4/-5 Vegetation Monitoring Instrument (VMI) (1.1-km SR), the IRS-1C/-1D Linear Imaging Self-Scanner (LISS)-III (23.5-m SR), IRS-P6 LISS-III (23.5-m SR), and IRS-P6 Advanced Wide Field Sensor (AWiFS) (56-m SR).
   b) The number of SSRC output spectral types reduces from 46 to 32, approximately equal to a 30% loss with respect to LSRC's.
   c) The expected effects of the loss in spectral resolution are the following.
      i) The loss of the B channel is expected to decrease the capability of detecting haze, smoke plumes, and water types [43], [46]. For the remaining spectral categories, the weights of the B channel are low in the LSRC decision-rule set to be insensitive to atmospheric effects (refer to Section II-B) [27], i.e., the importance of the B channel is not relevant in LSRC excluding the detection of classes haze, smoke plumes, and (in part) water.

TABLE III

IN THE x-AXIS: EQUIDISTANT BAND INDEXES MONOTONICALLY INCREASING WITH SPECTRAL WAVELENGTH, FROM VISIBLE B TO MIR (ALSO REFER TO TABLES I AND II). IN THE y-AXIS: TOARF VALUES IN RANGE $[0, 1] \times 100$ OF OPEN-SEA-WATER SPECTRAL SIGNATURES EXTRACTED FROM THE SAME SEA WATER REGION OF INTEREST LOCATED ACROSS THE FOUR RS IMAGES SHOWN IN FIGS. 8(A), 9(A), 10(A) AND 11(A). ABOUT THE ADOPTED NOTATION, ETM1 IDENTIFIES A LANDSAT-7 ETM+ BAND 1-LIKE IMAGE, AND SO ON, UP TO BAND ETM7, RANGING FROM VISIBLE B TO MIR, WHEREAS BAND ETM6, DEALING WITH THE TIR, IS OMITTED. FOR EXAMPLE, A SPOT-2/-5 BAND 1 IS APPROXIMATELY EQUIVALENT IN TERMS OF SPECTRAL SENSITIVITY CURVE TO ETM2, AN ASTER BAND 1 IS APPROXIMATELY EQUIVALENT TO ETM2, ETC.

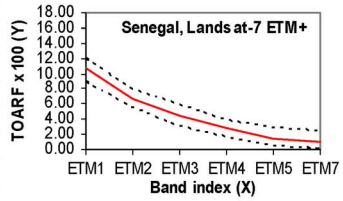

Senegal, Landsat-7 ETM+, 2000-11-06			
X	*Min Y*	*Max Y*	*Mean Y*
ETM1	9.00	12.00	10.68
ETM2	5.50	7.80	6.70
ETM3	3.10	5.88	4.44
ETM4	1.56	3.92	2.90
ETM5	0.40	2.74	1.32
ETM7	0.00	2.35	0.97

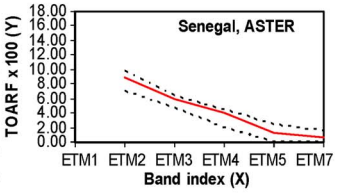

Senegal, ASTER, 2004-02-08			
X	*Min Y*	*Max Y*	*Mean Y*
ETM1			
ETM2	7.00	9.80	9.00
ETM3	4.70	6.40	5.88
ETM4	2.00	4.50	4.00
ETM5	0.00	2.30	1.24
ETM7	0.00	1.50	0.72

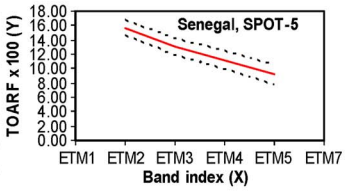

Senegal, SPOT-5, 2006-03-08			
X	*Min Y*	*Max Y*	*Mean Y*
ETM1			
ETM2	14.50	16.80	15.67
ETM3	11.70	14.10	13.05
ETM4	9.80	12.50	11.25
ETM5	7.80	10.50	9.17
ETM7			

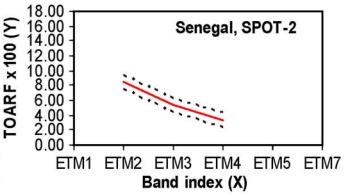

Senegal, SPOT-2, 2006-03-01			
X	*Min Y*	*Max Y*	*Mean Y*
ETM1			
ETM2	7.45	9.41	8.51
ETM3	4.31	6.27	5.40
ETM4	2.35	4.31	3.35
ETM5			
ETM7			

TABLE IV

REFERENCE SPECTRAL SIGNATURE IN TOARF VALUES (STRETCHED INTO RANGE {0, 255}): VEGETATED ARABLE LAND

Vegetated arable land – Landsat-7, ETM+, p191r030, Italy				
	Min	*Max*	*Mean*	*Stdev*
ETM1	31	36	32,53	0,83
ETM2	31	35	32,68	1,21
ETM3	23	32	26,86	1,65
ETM4	89	102	95,14	2,52
ETM5	36	45	41,31	2,25
ETM7	15	24	18,49	1,78
ETM62	126	128	127,00	0,53

TABLE V

REFERENCE SPECTRAL SIGNATURE IN TOARF VALUES (STRETCHED INTO RANGE {0, 255}): RANGELAND

Rangeland – Landsat-7 ETM+, p150r036, Pakistan				
	Min	*Max*	*Mean*	*Stdev*
ETM1	24	28	25,68	1,38
ETM2	22	29	25,68	1,89
ETM3	25	31	27,95	1,81
ETM4	57	84	70,68	5,81
ETM5	70	92	78,84	6,08
ETM7	42	58	48,05	4,14
ETM62	129	133	131,37	1,34

ii) The loss of the MIR2 channel is expected to decrease the capability of discriminating bare soil types, particularly burned areas. For example, several burned-area indexes employ MIR2 in comparison with the NIR channel [77]. However, in general, the weights of the MIR2 channel are low in the LSRC decision-rule set, employing a convergence-of-evidence approach [27], i.e., the importance of the MIR2 channel is not relevant in LSRC.

iii) The loss of the TIR channel is expected to increase the spectral confusion between light-toned (highly reflective) soil types, particularly in mountainous (and cold) areas, with classes thick and thin clouds (identified as TNCL and TKCL, respectively [27]) and either snow or ice spectral classes (identified as SN and ICSN, respectively [27]).

2) Four-band Advanced Very High Resolution Radiometer (AVHRR)-like SRC (AVSRC). The four spectral channels are R, NIR, MIR1, and TIR. The removed Landsat bands are B, G, and MIR2.
   a) The target satellite sensors are the National Oceanic and Atmospheric Administration (NOAA) AVHRR in satellite numbers 15–17 (1.1-km SR) and the Exploitation of Meteorological Satellites (EUMETSAT) Meteosat Second Generation (MSG, which is geostationary, acquired every 15 min, with 3-km SR).
   b) The number of AVSRC output spectral types reduces from 46 to 39, approximately equal to a 15% loss with respect to LSRC's. It is noteworthy that AVSRC guarantees the best compromise (ratio) between the number of detected spectral categories and acquired spectral channels as further proof of the relevance of and complementarity between the visible, NIR, MIR, and TIR portions of the electromagnetic spectrum.
   c) The expected effects of the loss in spectral resolution are the following.
      i) The loss of the B and G channels is expected to decrease the capability of detecting haze, smoke plumes, and water types (refer to the earlier discussion about SSRC).
      ii) About the loss of the MIR2 channel, refer to the earlier discussion about SSRC.
3) Five-band Advanced Along-Track Scanning Radiometer (AATSR)-like SRC (AASRC). The five spectral channels are G, R, NIR, MIR1, and TIR. The removed Landsat bands are B and MIR2.
   a) The target satellite optical sensors are the ENVISAT AATSR (1-km SR), the European Remote Sensing Satellite (ERS)-1 ATSR-1 (1-km SR), and the ERS-2 ATSR-2 (1 km SR).
   b) The number of AASRC output spectral types is the same as AVSRC's and therefore equal to 39 and approximately equal to a 15% loss with respect to LSRC's. This is due to the fact that the weight of channel G, which is present in AASRC but missing in AVSRC, is low in the LSRC decision-rule set based on convergence-of-evidence principles (refer to earlier discussion about SSRC).
   c) For the expected effects of the loss in spectral resolution, refer to earlier discussion about AVSRC.
4) Four-band IKONOS-like SRC (ISRC). The four spectral channels are B, G, R, and NIR. The removed Landsat bands are MIR1, MIR2, and TIR.
   a) The target satellite optical sensors are VHR, HR, and MR optical sensors, such as GeoEye-1 (MS: 1.64-m SR, PAN: 0.41-m SR), WorldView-2 (MS: 1.84-m SR, PAN: 0.46-m SR, and to be launched in 2009), QuickBird-2 (MS: 2.44-m SR, PAN: 0.61-m SR), PLEIADES-1/-2 (MS: 2.8-m SR, PAN: 0.7-m SR, and to be launched by the Centre National d'Etudes Spatiales (CNES) in 2009), IKONOS-2 (MS: 4-m SR, PAN: 1-m SR), OrbView-3 (MS: 4-m SR, PAN: 1-m SR), KOrean MultiPurpose SATellite (KOMPSAT)-2 (MS: 4-m SR, PAN: 1-m SR), TopSat (MS: 5-m SR, PAN: 2.5-m SR), RapidEye 1–5 (6.5-m SR, whose band 4, dealing with the Red Edge portion of the electromagnetic spectrum [45], is ignored by ISRC), FORMOsa SATellite (FORMOSAT)-2 (MS: 8-m SR, PAN: 2-m SR), Astrium SPOT-6/-7 (MS: 8-m SR, PAN: 2-m SR, and to be launched in 2012 and 2017, respectively), Advanced Land Observing Satellite (ALOS) Advance Visible and Near IR Radiometer type 2 (AVNIR-2) (10-m SR), and the Project for On-Board Autonomy-2 Compact High Resolution Imaging Spectrometer (PROBA; 20-m SR, to be launched in 2009; unfortunately, this sensor is not provided with an onboard calibration system and must rely on vicarious calibration) [78].
   b) The number of ISRC output spectral types reduces from 46 to 25, approximately equal to a 45% loss with respect to LSRC's.
   c) The expected effects of the loss in spectral resolution are the following.
      i) The loss of the MIR1 channel is expected to decrease the accuracy and reliability of the separation of 1) snow from cloud [80] and 2) vegetation and rangeland from bare soil types (also refer to Section V). Since its wavelengths are sensitive to water absorption, MIR1 is sensitive to both vegetation moisture content and soil moisture [79]. For example, in [79], the channel MIR1 is described as the best Landsat band overall.
      ii) About the loss of the MIR2 channel, refer to earlier discussion about SSRC.
      iii) The simultaneous loss of the TIR and MIR channels is expected to increase the spectral confusion between light-toned soil types with clouds and snow (refer to the previous discussion about SSRC).
   d) The discrete and finite sorted set of color-based semi-concepts detected by ISRC comprises five *parent* spectral categories (supercategories), which are listed next according to their order of presentation [to be compared with the six parent categories employed by LSRC (see Section II-D)]: 1) *either snow or ice or cloud or light-toned bare soil*; 2) *either water or shadow*; 3) *vegetation*; 4) *either bare soil or built-up*; and 5) *outliers*.

5) Three-band Disaster Monitoring Constellation (DMC)-like SRC (DSRC). The three spectral channels are G, R, and NIR. The removed Landsat bands are B, MIR1, MIR2, and TIR.
   a) The target satellite optical sensors are the Landsat-1/-2/-3/-4/-5 Multispectral Scanner [(MSS) 79-m SR, where band 3 of the MSS, dealing with the Red Edge portion of the electromagnetic spectrum [45], is ignored by DSRC), IRS-P6 LISS-IV (5.8-m SR), SPOT-1/-2 HRV (MS: 20-m SR, PAN: 10-m SR), and DMC, namely, Alsat-1 (32-m SR), Deimos-1 (22-m SR), Beijing-1 (MS: 32-m SR, PAN: 4-m SR), UK-DMC (32-m SR), UK-DMC2 (22-m SR), and Nigeria Sat-1 (32-m SR) SLIM6 instrument.
   b) The number of DSRC output spectral types is the same as ISRC's, which is equal to 25 and approximately equal to a 45% loss with respect to LSRC's. This is due to the fact that the weight of channel B, which is present in ISRC but missing in DSRC, is low in the LSRC decision-rule set based on convergence-of-evidence principles (refer to aforementioned discussion about SSRC).
   c) For the expected effects of the loss in spectral resolution, refer to the previous discussion about ISRC. For the loss of the B band, refer to earlier discussion about SSRC.

It is noteworthy that, since LSRC is pixel based, i.e., it works at the sensor resolution, the integrated SRC system of systems, comprising LSRC together with its five downscaled versions, can be considered multisource and multiresolution, in agreement with the visionary goals of a GEOSS [17].

IV. LSRC Scalability to the SPOT and IRS Satellite Sensor Series: The Problem of Absolute Radiometric Calibration Zero-Value Offset Parameters

The GEO-CEOS international QA4EO guidelines require the following: 1) an appropriate coordinated program of Cal/Val activities throughout all stages of a spaceborne mission, from sensor build to end of life, and 2) metrological/statistically based quality indicators, provided with a degree of uncertainty in measurement, to be established for every sensor-derived data product [17]. For example, the radiometric calibration uncertainty of TOARD values generated from the Landsat-5 MSS, Landsat-5 TM, and Landsat-7 ETM+ sensors is known to be between 5% and 10% [82]. Unfortunately, in existing literature, these authors were unable to find any radiometric quality and uncertainty estimate of the popular SPOT and IRS sensor series [83]. Despite the fact that it is rarely a subject of concern by the RS community [84], the lack of SPOT and IRS data quality assurance represents a potential limitation on the applicability domain of the operational automatic integrated SRC system of systems and, in general, on the development of operational satellite-based measurement systems [for which the rule "garbage in, garbage out" holds (see Section I)]. Therefore, in agreement with the international QA4EO guidelines, this section further investigates the radiometric quality and stability of the SPOT and IRS sensor families.

To the best of our knowledge, offset parameters $B(b)$, $b = 1, \ldots, Bnd$, provided by the SPOT metadata DIMAP file to be employed in (1.1), appear to be constant with time and equal to zero. This is acknowledged by SPOT Image in a personal communication [81] and, to some respect, by existing literature. For example, in [12], Richter writes that, in the SPOT metadata files, "the standard offset values are zero." In [38], which specifically deals with the SPOT-4 VEGETATION and HRVIR onboard calibration systems and vicarious calibration methods over test sites, the offset calibration term $B(b)$ is omitted from (1.1). This means that, in the words of an anonymous referee, the SPOT DNs "are assumed to be already equalized and corrected by a dark-object current." If so, a $B(b)$ "offset parameter is used only if, after the DN equalization step, a dynamic adaptation is required." If no dynamic adaptation is applied, then $B(b) = 0$, which appears to be always the case. This referee's explanation is not supported by the text in [38] where keywords such as "offset," "dark (object)," "black (object)," and "equalization" are absent.

Based on the authors' experience, zero-value offset parameters are always retrieved from the IRS metadata files, too. In [12], Richter writes that, in the three optical sensors carried onboard the IRS-P6 platform, the bias "nominal value is zero... the calibration coefficient seem to be constant with time, i.e., independent of the scene, based on laboratory calibration."

The first author of this paper also observed zero-value offset parameters in seven out of seven RapidEye image metadata files available.

To summarize, according to the authors' experience supported by Richter's observations, a list of currently ongoing European and non-European EO satellite optical imaging sensor series employing, in practice, absolute calibration zero-value offset parameters is provided as follows: 1) SPOT-1/-2 HRV; 2) SPOT-4 HRVIR; 3) SPOT-5 HRG; 4) SPOT-4/-5 VMI 1 and 2; 5) IRS-1C/-1D LISS-III; 6) IRS-1C/-1D WiFS; 7) IRS-P6 LISS-III; 8) IRS-P6 AWiFS; and 9) RapidEye.

Are the SPOT and IRS zero-value offset parameters, which are apparently generated from laboratory calibration (according to the Richter conjecture), validated in terms of calibration quality and uncertainty in agreement with the QA4EO initiative? This subject is discussed in the following sections (about RapidEye imagery, our radiometric quality indexes cannot be considered statistically significant).

A. SPOT

In literature, Richter states that, in the SPOT metadata files, "the standard offset values are zero. Occasionally, however, for SPOT-4/-5 data, a slightly negative offset has to be introduced for band 4 (1.6-μm MIR) in cases when the scene water reflectance is too high (it should be close to zero)" [12, p. 100]. In [38], it is stated that "the absolute calibration consists in estimating and monitoring the parameter A_k for the kth spectral band considered. For many applications, the most important thing is not the absolute calibration but the relative calibration between images of the same instrument at different dates (multidate calibration), images acquired simultaneously in different spectral bands (interband calibration), and images acquired

by two different sensors (namely, SPOT-4 VEGETATION and HRVIR sensor intercalibration)." The authors of this paper, together with an anonymous referee, disagree with this quoted statement. In the words of this anonymous referee, "absolute calibration is the establishment of the 'Gain' and 'Offset,' not simply a ratio" (generated from relative calibration). In line with the Richter experience (refer to previous discussion) [12], these authors have observed that, in several SPOT-4 and SPOT-5 scenes radiometrically calibrated into TOARF values, computed by (1.1) and (1.3) as a function of the absolute radiometric calibration parameters retrieved from the SPOT DIMAP metadata files, scene-derived land-cover-class-specific spectral signatures in TOARF values 1) may fall well outside the range of change of the same land-cover-class-specific TOARF values detected across time and space by a plethora of spaceborne optical sensors, such as those listed in Tables I and II, and 2) appear to be inconsistent with library or ground-measured surface-reflectance spectra [73], [80] that should fall (as ideal atmospheric-noise-free instances) within the range of variation of scene-derived land-cover-class-specific spectral signatures in TOARF values affected by atmospheric effects (refer to Sections II-D and III). These two types of inconsistencies are illustrated in the following example, which is representative of many similar cases personally experienced by the authors.

Four open-sea-water-specific (equivalent to a dark object) spectral signatures in TOARF values, shown in Table III, are extracted from the same region of interest located across a multisensor image data set consisting of a Landsat-7 ETM+, one SPOT-5 HRG, one ASTER, and one SPOT-2 HRV image of the Low Casamance mangrove ecosystem in Senegal acquired on November 6, 2000, March 8, 2006, February 28, 2004, and March 1, 2006, respectively (see Figs. 1(a), 2(a), 3(a) and 11(a) in Part II of this paper). In the target region of interest, no sun-glint phenomenon occurs, and atmospheric scattering appears negligible in the visible and NIR portions of the electromagnetic spectrum sensitive to the presence of haze and aerosols, whereas the amount of atmospheric scattering occurring at the MIR region of the electromagnetic spectrum is known to be "quite small except for very hazy atmospheres and can be considered negligible" [43, p. 476]. In Table III, the Landsat channels 1 to 7, identified as ETM1 to ETM7, respectively, are adopted as a reference in the comparison of multisensor channels featuring (approximately) the same sensitivity curve [e.g., a Landsat-like band 7 is synthesized by an OR combination of channels 5, 6, 7, and 8 by ASTER (refer to Table I)]. In other words, these authors realize that the spectral bandwidth of the individual bands affects the amount of at-sensor radiance, but differences in the spectral bandwidth are considered negligible here. In addition, intersensor TOARD and TOARF value comparison should take calibration uncertainties into account, in agreement with guidelines for evaluating uncertainty of measurement found in the QA4EO documentation [17]. For example, the calibration uncertainty of the Landsat-7 ETM+ TOARD values are $\pm 5\%$ [82]. Unfortunately, in existing literature, these authors were unable to find any calibration uncertainty estimate for the ASTER and SPOT sensors involved with the present comparison.

Table III shows that, in the proposed qualitative example, 1) SPOT-5 TOARF values fall well outside the range of change of the corresponding TOARF values detected by the Landsat-7 ETM+, ASTER, and SPOT-2 optical sensors; the relative increase in the band-specific SPOT-5 TOARF values with respect to the other sensors' values may be as high as 200% for band ETM2 up to 700% for band ETM5, which is far above the typical calibration uncertainty of spaceborne optical sensors (below 10% for the several Landsat sensors, as discussed previously), and 2) SPOT-5 TOARF values do not include, as their ideal atmospheric-noise-free realizations, surface-reflectance values of clear and turbid water types found in existing literature (e.g., refer to [80, p. 273]).

Overall, these authors have observed that SPOT-4/-5 overestimation of TOARD/TOARF values may occur imagewide at varying geographic positions and solar elevation angles. Therefore, SPOT-4/-5 radiometric overestimation is not due to geometric effects or local surface conditions and is far superior to typical values of calibration uncertainty (see earlier discussion). To summarize, the nature of SPOT-5 radiometric calibration inaccuracy appears to be accidental and scene dependent, such as out-of-band leakage effects [85].

B. IRS

About the calibration quality of the IRS sensor series, Richter observed that, in the three optical sensors carried onboard the IRS-P6 platform, the bias "nominal value is zero... the analysis of a couple of scenes showed that a nonzero bias is required to obtain reasonable surface-reflectance spectra... A fine tuning of the calibration coefficients may be necessary to obtain better agreement between scene-derived surface-reflectance spectra and library or ground measured spectra" [12, p. 104]. In line with this statement by Richter, these authors have encountered several IRS image instances whose radiometric calibration quality appears troublesome. Nonetheless, based on experimental evidence collected over more than two-thousand SPOT and IRS images processed in the framework of the IMAGE2006 European mosaic project conducted by the EC-Joint Research Center as part of the EU GMES Fast-Track Service Land Monitoring project [86], these authors consider the combination of nonzero gain parameters with zero-value offset parameters more accurate and stable in IRS imagery rather than in the SPOT-4/-5 images. As a consequence, in the IMAGE2006 mosaic project, IRS images have been preferred to SPOT-4/-5 imagery whenever the former were available and free of clouds (refer to Fig. 16 in Part II of this paper).

C. Comments

In agreement with the new QA4EO guidelines, the current vagueness about the SPOT and IRS calibration quality and uncertainty should be the subject of further inquiries by the RS community at the earliest opportunity and at the highest official level, such as the GMES bureau and the CEOS WGCV. On a personal basis, for the sake of truth and in the interest of the RS community involved with the development of operational satellite-based measurement systems, the first author of this

paper would personally welcome a comment by SPOT Image and the Indian Space Research Organisation about the aforementioned SPOT and IRS Cal/Val-related issues.

In common practice, until the calibration quality and uncertainty of SPOT-4/-5 and IRS data remains unknown, a community-agreed RS data preprocessing protocol comprising a relative calibration step in series with the absolute radiometric calibration of SPOT-4/-5 (and maybe IRS) imagery should be considered mandatory. For example, a user-driven standard dark-object subtraction, typically used to remove the additive atmospheric scattering (haze) effects [43], can be scheduled in series with (1.1), e.g., refer to [79]. In dark-object subtraction techniques, the DN to subtract from each band may be the band minimum, an average based upon a user-defined region of interest (typically, a water body of invariant spectral properties, a shadow area, or a black object featuring 0% reflectance), or a specific value to be user defined (e.g., selected from the DN frequency histogram of the whole RS image) [43], [73]. In this experiment, if a dark-object subtraction is employed in series with the linear equation (1.1), then the SPOT-5 image in $TOARF = (1.3)$ values, shown in Fig. 2(a) in Part II of this paper, provides an SRC map, shown in Fig. 2(b) in Part II of this paper, consistent with the SRC maps, shown in Figs. 1(b), 3(b) and 11(b) in Part II of this paper, generated from the radiometrically calibrated Landsat, ASTER, and SPOT-2 images, respectively.

If no relative calibration step is scheduled in series with the absolute radiometric calibration of SPOT-4/-5 (and maybe IRS) imagery, the SPOT-4/-5 (and maybe IRS) unknown radiometric quality and uncertainty must be coped with by scene-by-scene data-processing approaches which are intrinsically unsuitable for applications such as follows:

1) quantitative estimates of either physical (e.g., LAI) or biochemical variables [e.g., fraction of absorbed photosynthetically active radiation (FAPAR)], such as those provided in the frame of the VEGETATION For Africa (VGT4AFRICA) project,[6] led by the Flemish Institute for Technological Research NV (VITO), based on the SPOT-4/-5 VEGETATION sensor series [82];
2) operational automatic generation of standardized, advanced, and validated information products (e.g., classification maps) generated across time (e.g., image time series), space (e.g., image mosaics), and sensors as those required by the GEOSS and GMES programs;
3) photointerpretation of image data sets acquired across time and space in scientific applications such as land cover change detection at geographic scales ranging from local (areas up to 100 000 km^2) to global.

The obvious drawback of a SPOT-4/-5 (and maybe IRS) data-processing chain which includes a manual or semiautomatic missing offset parameter retrieval subsystem is that its operational performance measurement [in terms of ease of use, cost, and timeliness (refer to Section I)] becomes inferior to that of alternative spaceborne data sensors provided with complete and reliable absolute radiometric calibration offset and gain parameters.

V. LSRC Scalability to VHR Satellite Sensors: The Problem of VIs

Unfortunately, according to [27], the spectral resolution of popular VHR spaceborne optical sensors, such as GeoEye-1, IKONOS-2, QuickBird-2, and OrbView-3, which ranges from visible B to NIR wavelengths (from approximately 0.45 to 0.90 μm), seems unsuitable to support a downscaled version of LSRC. This is due to the well-known fact (but often forgotten in RS common practice [36]) that the lone normalized difference VI (NDVI), defined as

$$NDVI \in [-1, 1] = (NIR - R)/(NIR + R) \qquad (1.6)$$

by measuring the contrast between channels NIR and R, is unable, *per se*, to guarantee a robust (i.e., reliable and image independent) discrimination between vegetation and nonvegetation surface types [27], [45], [87]. Incidentally, the one-class dichotomous vegetation/nonvegetation classification problem represents the first decision level in any dichotomous hierarchical RS data classification taxonomy such as the Coordination of Information on the Environment (CORINE) [34], the USGS classification hierarchy [42], and the Food and Agriculture Organization of the United Nations (FAO) Land Cover Classification System (LCCS) [88]. In other words, if the vegetation/nonvegetation dichotomous classification of an RS image is not reliable, the land-cover-class taxonomies listed previously cannot be applied in RS common practice.

In general, with regard to spectral VIs, it is well known that the following are true.

1) In general, band ratioing causes a loss in spectral resolution, which is a drawback in MS image classification [40].
2) Starting from a given canopy radiative transfer model, the so-called operational statistical methods provide an estimate of canopy biophysical/biochemical variables, such as the LAI and the FAPAR absorbed by canopy, from a variety of MS VIs [45, p. 286]. The basic assumption about VIs is that some algebraic combination of RS spectral bands should be as follows:
   a) sensitive to target vegetation factors such as vegetation structure (leaf density and distribution) and the state of vegetation cover (leaf water content, leaf chlorophyll content, age, mineral deficiencies, parasitic attack, etc.);
   b) insensitive to other nonvegetation factors affecting spectral reflectance, namely, soil background properties, solar/viewing geometry, and atmospheric conditions.
3) Various VIs, to be linearly related to LAI, require DNs to be converted into TOARF rather than TOARD values [45, p. 271] (also refer to Section II-B). Unfortunately, this recommendation is rarely heeded by RS practitioners.

[6]The VGT4AFRICA project received funding from the 6th Framework Program (FP6) of the European Commission. The VGT4AFRICA project aims at setting up an operational and timely distribution system of VEGETATION data (http://www.spot-vegetation.com) from the SPOT satellites and high-level derived products to all African countries in the framework of GMES [8].

4) The advantages of NDVI are the following.
   a) $NDVI \in [-1, 1]$; thus, it is dimensionless and finite ranged and, therefore, intuitive and easy to use.
   b) It can be effective in predicting surface properties when vegetation canopy is not too dense or too sparse [45, p. 250].
5) The well-known limitations of NDVI are the following.
   a) If a canopy is too sparse (i.e., the LAI is low), the background signal (e.g., soil reflectance) can change the NDVI significantly.
   b) If the canopy is too dense (i.e., LAI is large), NDVI saturates.
   c) The relationship between LAI and NDVI, the latter being computed from TOARD or TOARF, is nonlinear [45, p. 271].
6) The dimensionless vegetation ratio index

$$VRI \in (0, \infty) = NIR/R = (1 + NDVI)/(1 - NDVI) \tag{1.7}$$

   is much slower to saturate than NDVI when a canopy is dense, i.e., it can enhance the contrast between soil and vegetation while minimizing the effects of illumination conditions (shadow areas). However, it is affected by soil reflectance underneath the canopy [45, p. 252]. Nonetheless, it has also been used for estimating LAI. In practice, VRI is inversely related to the chlorophyll absorption minimum which decreases with the canopy chlorophyll absorption, i.e., VRI increases with the canopy chlorophyll content.
7) As a consequence of the drawbacks listed earlier, several soil-adjusted VIs (SAVIs) have been proposed. For example, second derivatives around the red edge inflection point [(REIP); defined as the wavelength where the first derivative of the spectral reflectance curve reaches its maximum value], located between visible R and NIR spectra (called *red edge* reflectance characteristics), are proven to be linearly related (much better than VRI and NDVI) to LAI regardless of the canopy background (e.g., burned and unburned [45, p. 278]).

In line with the aforementioned statements and moving further from [27],[7] an intuitive strategy to remove soil effects from VRI is to replace VRI, equivalent to a first-order derivative, with a second-order derivative centered on the NIR waveband as follows (obviously, three bands are needed):

$$\begin{aligned}&\text{(Downward) Concavity centered on the NIR waveband}\\&= \text{Greenness}(R, NIR, MIR) \in [0, \infty)\\&= \max\{0, (NIR/R) + (NIR/MIR_{1.55-1.75})\\&\qquad -(R/MIR_{1.55-1.75})\}\\&\geq 0\end{aligned} \tag{1.8}$$

such that the following are satisfied.

1) Equation (1.8) is alternative to the greenness second linear function in the (sensor-specific, prior-knowledge-based, and image-independent) Tasseled Cap transformation of data generated by the Landsat-5 TM [18, p. 204] or Landsat-7 ETM+ [45, p. 260] (also refer to [27, Table 2]) sensors, where greenness is approximately equivalent to a contrast between channels NIR/(visible bands OR the MIR channel).
2) The first term in (1.8), i.e., $VRI = (NIR/R) \in (0, \infty)$, features the well-known properties described previously. It is related to the greenness second linear function in the Tasseled Cap transformation of the Landsat data (refer to the previous comment).
3) The second term in (1.8), i.e., $(NIR/MIR_{1.55 \div 1.75})$, is inversely related to the normalized difference of the bare soil index (NDBSI) adopted in [27] and directly related to the so-called Aerosol-Free VI $AFVI = (NIR - 0.66 * MIR_{1.55 \div 1.75})/(NIR + 0.66 * MIR_{1.55 \div 1.75}) \in [-1, 1]$ [45, p. 257]. However, unlike the first term in (1.8), which is sensitive to the canopy chlorophyll content, this second term is inversely related to the water absorption minimum which decreases with canopy water absorption, i.e., the term $(NIR/MIR_{1.55-1.75})$ increases with the canopy water content [45]. It is to be pointed out that AFVI is very similar to the Gao normalized difference water index $NDWI_{\text{Gao}} = (NIR - MIR)/(NIR + MIR) \in [-1, 1]$, where the term water index is rather vague and, unfortunately, quite misleading as it rather deals with canopy water content [89], [90]. In turn, $NDWI_{\text{Gao}}$ is equivalent to the so-called Wilson normalized difference moisture index $NDMI_{\text{Wilson}}$, where the term moisture is also rather vague, as it does not refer to soil moisture but to canopy water content [91]. The second term in (1.8) is also related to the wetness third linear function in the Tasseled Cap transformation of the Landsat data, particularly in the case of data from the Landsat-5 TM [18, p. 204], which appears as a contrast between channels (visible OR NIR)/MIR.
4) The third term in (1.8), i.e., $(R/MIR_{1.55-1.75})$, is directly related to the wetness Tasseled Cap component [45, p. 260], to the normalized difference snow index adopted in [27], and to the so-called modified normalized difference water index defined by McFeeters as $NDWI_{\text{McFeeters}} = (G - MIR)/(G + MIR) \in [-1, 1]$ [91], suitable for separating water from built-up land (whose response in the MIR band tends to be greater than or equal to the response in visible G, unlike that of water). It is noteworthy that, in (1.8), the negative third term (also called snow index) is adopted to reduce the greenness index value in snow/ice areas where the second term $(NIR/MIR_{1.55-1.75})$ would rather tend to be quite large. The drawback of introducing this negative third term is that (1.8) loses sensitivity in detecting vegetation in shadow areas.

To summarize, the greenness index computed via (1.8) is quite different from the greenness Tasseled Cap component

[7] In [27, p. 2585], it is written that "vegetation-specific spectral properties require conditions ($Vis \ll NIR$) and ($NIR \gg MIR$), equivalent to conditions (NDVI is *high*) and (NDBSI is *low*)," where the normalized difference bare soil index (NDBSI) is defined as $NDBSI = (MIR_{1.55-1.75} - NIR)/(MIR_{1.55-1.75} + NIR)$.

of the Landsat-5 TM [18, p. 204] or Landsat-7 ETM+ [45, p. 260] imagery (also refer to [27, Table II]). Rather, it should be considered an original combination of three well-known spectral indexes whose physical meaning is sometimes fuzzy in existing RS literature, namely, as follows:

1) a canopy chlorophyll absorption index;
2) a canopy water absorption index;
3) a snow/water ratio index.

It is noteworthy that the algebraic sum of the first two terms of (1.8) is equivalent to a second-order derivative, centered on the NIR waveband, monotonically increasing with both canopy chlorophyll content and canopy water content. As a consequence, from a theoretical standpoint and in line with [45, p. 278], this sum is expected to be linearly related (much better than VRI and NDVI) to LAI, irrespective of canopy background (e.g., burned and unburned).

A sensor-specific implementation of (1.8) can benefit from the approximation of a second- and first-order derivative of the discrete wavebands (as reported in [45, p. 278]). For example, in the Landsat case, (1.8) becomes

$$\begin{aligned}\text{Greenness} &= [2./(1.650-0.660)] \\ &\quad * [(NIR_{0.76\div0.90}-Red_{0.63\div0.69})/(0.830-0.660) \\ &\qquad +(NIR_{0.76\div0.90}-MIR_{1.55\div1.75})/(1.650-0.830)] \\ &\quad -[(Red_{0.63\div0.69}-MIR_{1.55\div1.75})/(1.650-0.660)]\end{aligned} \tag{1.9}$$

where

0.660 μm full width at half maximum (FWHM) value of band (E)TM3 (Visible R) in the range [0.63, 0.69] μm;
0.830 μm FWHM of band (E)TM4 (NIR) in the range [0.76, 0.90] μm;
1.650 μm FWHM of band (E)TM5 (MIR1) in the range [1.55, 1.75] μm.

Let us compare the greenness estimate computed via (1.8) against two traditional VISs, namely, NDVI and VRI, generated from four reference spectral signatures radiometrically calibrated into TOARF values linearly stretched from range [0, 1] into range {0, 255} (see Tables IV–VII and Fig. 5). Tables VIII and IX show that the proposed greenness index is the least affected by the variable soil reflectance underneath the vegetation canopy. In fact, if the canopy is dense (i.e., if LAI is large), the greenness index boosts without saturating (better than VRI) in both absolute and relative terms (refer to Tables VIII and IX, respectively). The difference in greenness values between the dense and the sparse canopy (rangeland) is superior (in both relative and absolute terms) to that in the VRI domain, while the difference in greenness values between the sparse canopy and the bare soil remains superior (in absolute terms, 1.48 versus 1.18) to that in the VRI domain.

To summarize, *R, NIR, and MIR wavelengths are equally important in computing the second derivative of canopy reflectance around the REIP* [45]. In other words, all these bands are fundamental in pursuing the reliable detection of the

TABLE VI
REFERENCE SPECTRAL SIGNATURE IN TOARF VALUES (STRETCHED INTO RANGE {0, 255}): PLOWED FIELDS

Ploughed fields – Landsat-7, ETM+, p197r021, Denmark				
	Min	*Max*	*Mean*	*Stdev*
ETM1	41	45	42,96	1,01
ETM2	45	49	46,82	0,92
ETM3	53	60	56,84	1,67
ETM4	74	81	77,18	1,69
ETM5	78	88	83,04	2,63
ETM7	45	54	50,46	2,19
ETM62	134	136	135,00	0,35

TABLE VII
REFERENCE SPECTRAL SIGNATURE IN TOARF VALUES (STRETCHED INTO RANGE {0, 255}): SNOW

Snow – Landsat-7 ETM+, p149r036, Pakistan.				
	Min	*Max*	*Mean*	*Stdev*
ETM1	90	169	153,05	16,83
ETM2	90	172	151,87	17,86
ETM3	91	171	156,90	18,87
ETM4	94	182	158,91	20,01
ETM5	6	29	12,48	3,01
ETM7	4	26	9,39	2,77
ETM62	97	101	99,91	0,94

dichotomous vegetation/nonvegetation classification problem which constitutes the basis of any hierarchical classification taxonomy (e.g., the USGS classification hierarchy [42] and FAO's LCCS [88]). This consideration implies the following.

1) Due to their lack of spectral resolution, VHR and HR satellite sensors, such as GeoEye-1, WorldView-2 (to be launched), QuickBird-2, PLEIADES-1/-2 (to be launched), IKONOS-2, OrbView-3, KOMPSAT-2, TopSat, RapidEye, FORMOSAT-2, Astrium SPOT-6/-7 (to be launched), and ALOS AVNIR-2 (refer to Section III), are expected to be difficult to classify with a high degree of confidence by a preliminary automated spectral knowledge-based classifier starting from the dichotomous vegetation/nonvegetation classification problem [42], [88]. In fact, an automatic RS image spectral-rule-based decision-tree classifier, as is LSRC, must rely upon uncorrelated and redundant sources of spectral evidence to generate plausible semantic conjectures based on convergence-of-evidence inference strategies. Thus, to compensate for their scantiness in spectral resolution, VHR imagery may require a two-stage classification system comprising, in cascade, a pixel-based preliminary classification first stage and a second-stage stratified image data-driven classifier, either semiautomatic or self-supervised, such as [92], or a second-stage stratified class-specific rule-based classifier exploiting contextual properties (refer to Section II-C3b).
2) Next-generation satellite sensors, such as FIEOSs (refer to Section II-B) [48], [49], should provide a careful combination of spatial and spectral resolution fine enough to allow the automatic solution of the dichotomous vegetation/nonvegetation mapping problem found at the

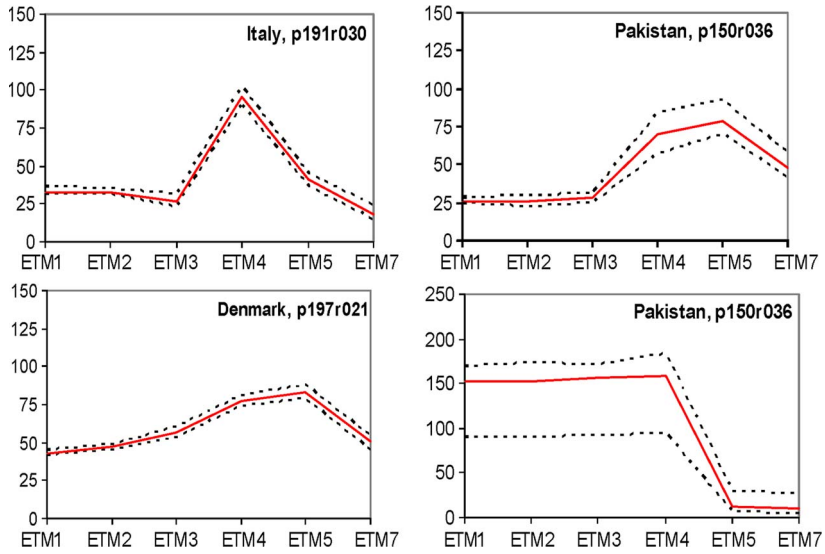

Fig. 5. Reference spectral signatures in TOARF values (scaled into the discrete range {0, 255}). (From left to right and top to bottom) Vegetated arable land, rangeland, ploughed fields, and snow. Refer to Tables IV–VII, respectively.

TABLE VIII
VIs EXTRACTED FROM REFERENCE SPECTRAL SIGNATURES IN TOARF VALUES (STRETCHED INTO RANGE {0, 255}): VEGETATED ARABLE LAND, RANGELAND, PLOWED FIELDS, AND SNOW CASE STUDIES

	Vegetation	*Rangeland*	*Bare soil*	*Snow*	*Mean*	*StDev*
Greenness	3.54+2.30 - 0.65 = 5.19	2.53+0.89 - 0.35 = 3.07	1.35+0.92 - 0.68 = 1.59	1.05 + 12.73 – 12.57 = 1.21	2.76	1.80
NDVI	0.56	0.43	0.15	0.006	0.28	0.25
VRI	3.54	2.53	1.35	1.05	2.11	1.14

TABLE IX
STANDARDIZED VIs (FEATURING ZERO MEAN AND UNIT VARIANCE) EXTRACTED FROM THE SET OF REFERENCE SPECTRAL SIGNATURES IN TOARF VALUES (STRETCHED INTO RANGE {0, 255}): VEGETATED ARABLE LAND, RANGELAND, PLOWED FIELDS, AND SNOW CASE STUDIES

	Vegetation	*Rangeland*	*Bare soil*	*Snow*	*Mean*	*StDev*
Stand. Greenness	1.34	0.17	-0.65	-0,86	0	1
Stand. NDVI	1.08	0.57	-0.54	-1,11	0	1
Stand. VRI	1.24	0.36	-0.67	-0.93	0	1

first decision level in hierarchical RS image classification taxonomies, such as the USGS [42] and the FAO LCCS [88]. In particular, any increase in SR across visible and NIR channels while removing the MIR band(s) is expected to reduce the accuracy and degree of confidence of the one-class vegetation mapping capability, which may be the case for the future PLEIADES-1/-2 and Astrium SPOT-6/-7 missions in comparison with ongoing SPOT-4/-5 sensors.

VI. SUMMARY AND CONCLUSION

This paper has reviewed several RS-IUS architectures found in existing literature. A novel family of RS-IUSs, called the Shackelford and Davis two-stage stratified hierarchical RS-IUS model, has been highlighted. An innovative operational fully automated LSRC system, recently presented in RS literature, has been considered eligible for use as the automatic pixel-based preliminary classification first stage in a two-stage stratified hierarchical RS-IUS architecture. As input, LSRC requires a seven-band Landsat-like image radiometrically calibrated into TOARF or surface-reflectance values, the latter being an ideal (atmospheric-noise-free) case of the former.

To be input with RS images acquired by spaceborne and airborne data sources different from the Landsat sensor series, five original downscaled versions of LSRC, identified as SSRC, AVSRC, AASRC, ISRC, and DSRC, have been proposed. Comprising LSRC, together with its five novel downscaled implementations, the integrated operational automatic SRC system of systems employs as input a radiometrically calibrated MS image acquired by almost any of the ongoing or future planned satellite optical missions.

Several general conclusions of potential interest to the RS community stem from this paper.

1) There is experimental evidence that the absolute calibration of SPOT-4/-5 (and, perhaps, IRS) images into TOARD values and, as a consequence, TOARF and surface-reflectance values may not be considered reliable due to the lack of offset parameters in these image calibration metadata files. This means that, in many practical cases, an additional relative calibration step (e.g., dark-object subtraction) is recommended in series with the SPOT-4/-5 (and, perhaps, IRS) absolute radiometric calibration stage (refer to Section IV).
2) A novel greenness index, better correlated to LAI than the ordinary NDVI, is computed from an MS image radiometrically calibrated into TOARF values (refer to Section V).
3) Satellite sensors provided with visible B, G, and R channels plus a NIR channel, such as the popular VHR satellite sensors GeoEye-1, IKONOS-2, and QuickBird-2 [plus many others (see previous discussion)], feature an average interband correlation qualitatively estimated as high ($\geq$ 0.8; refer to the qualitative partition of correlation values into fuzzy sets low, medium, and high

by Congalton [69]) across the three visible portions of the electromagnetic spectrum (also refer to experimental work in Part II of this paper). Thus, these sensors are expected to be difficult to deal with by a preliminary automatic spectral knowledge-based classifier, such as SRC, which must rely upon uncorrelated and redundant sources of spectral evidence to generate plausible semantic conjectures based on a convergence-of-evidence inference strategy. In particular, when no MIR channel is available, a) the dichotomous vegetation/nonvegetation class recognition capability based on spectral properties alone lacks accuracy and reliability [refer to earlier point 2)] and b) the spectral separation between snow and clouds becomes extremely difficult or impossible, as clearly acknowledged by existing literature [80]. Therefore, to separate vegetation from nonvegetation and snow from clouds, additional image features, such as texture and shape, are expected to be taken into consideration by the battery of second-stage stratified class-specific classification modules employed in two-stage stratified hierarchical RS-IUS instantiations suitable for automatic VHR image interpretation (refer to Section II-C3). In general, irrespective of SR, when spectral resolution diminishes, the length and computational complexity of the processing chain implemented in automatic RS-IUS instantiations increase. For the same reasons, it is possible to conclude that future planned EU satellite missions, such as PLEIADES-1/-2 and the follow-on missions Astrium SPOT-6/-7, are moving farther away than the SPOT-4/-5 sensor series from the development of onboard automatic image-processing capabilities required by so-called future fourth-generation intelligent EO satellites (refer to Section V).

Specific conclusions about the integrated SRC system of systems are listed next (refer to Section IV).

A) To the best of our knowledge and in line with the international QA4EO guidelines, the integrated SRC system of systems constitutes the sole example of an operational fully automated RS image mapping system requiring neither user-defined parameters nor reference data samples to run upon a radiometrically calibrated MS image acquired across time, space, and sensors.
B) From the computational point of view, SSRC, AVSRC, AASRC, ISRC, and DSRC, featuring a downscaled LSRC rule set, are expected to be more efficient than the near-real-time LSRC which requires less than 5 min for calibration and classification of a Landsat scene in a C++ programming language implementation.
C) Due to its inferior spectral resolution, SSRC is provided with a spectral category discrimination capability inferior to LSRC's by about 30% (from 46 to 32 spectral categories).
D) Due to its inferior spectral resolution, AVSRC is provided with a spectral category discrimination capability inferior to LSRC's by about 15% (from 46 to 39 spectral categories). AVSRC also applies to MSG images that are geostationary and acquired every 15 min. This opens a wide scenario of real-time image-mapping applications for early warning systems such as flood detection, cloud detection, fire detection, smoke-plume detection, etc., as possible alternatives to or in combination with the MSG products and services currently supported by EUMETSAT [93].
E) AASRC is provided with the same spectral category discrimination capability of AVSRC. AASRC may be of specific interest to ESA whose aim is to develop a semantic-based query of the AATSR image data archive in the Service Support Environment portal [94].
F) Due to its inferior spectral resolution, ISRC is provided with a spectral category discrimination capability inferior to LSRC's by about 45% (from 46 to 25 spectral categories). Provided with no MIR channel, its spectral resolution can be considered theoretically insufficient to separate, with high accuracy and reliability, vegetation from nonvegetation and snow from clouds based on spectral properties alone [see earlier comment 3)]. On the other hand, owing to the VHR of its input imagery, ISRC paves the way, together with SSRC (see aforementioned comments), to the automatic classification of VHR imagery where man-made structures and infrastructures are distinguishable, e.g., refer to [21], [26], [32], [47], [61], [95], and [96]. The proposed automatic VHR RS-IUS instantiation consists of a two-stage stratified hierarchical RS-IUS architecture whose preliminary classification first stage is implemented as an automatic integrated SRC system of systems (refer to Section II-C3). This VHR image understanding approach is alternative to OBIA, which is currently considered the state-of-the-art in commercial image-processing software toolboxes.
G) Due to its inferior spectral resolution, DSRC is provided with a spectral category discrimination capability equal to ISRC's, therefore inferior to LSRC's by about 45% (from 46 to 25 spectral categories). Like ISRC, it is provided with no MIR channel; therefore, its spectral resolution can be considered theoretically insufficient to separate, with high accuracy and reliability, vegetation from nonvegetation and snow from clouds based on spectral properties alone [see comment 3)]. DSRC can be theoretically employed with RS imagery consisting of only two channels, namely, one visible and one NIR channel.

Worthy of note is that, in recent years, a recreational (artistic and cosmetic) rather than scientific (quantitative) application of VHR (e.g., IKONOS-2 and QuickBird-2) and HR (e.g., SPOT-4/-5) spaceborne imagery has experienced a remarkable growth in popularity among RS scientists, practitioners, and nonscience user communities due to the development of Web-based geobrowsers, such as Google Earth, NASA's World Wind, and Microsoft's Virtual Earth. The aim of commercial Web-based map servers and geobrowsers is to use geography as a way of searching and viewing spatial information, i.e., to search for information provided with a geographic footprint [108]. To reach their goal, geobrowsers must rely upon multisource multiresolution RS image databases at global scale

whose location error is below a given project requirement, but whose radiometric quality may be even inferior to that required by manual scene-by-scene interpretation of RS image mosaics which is, in turn, inferior to the radiometric calibration required by operational satellite-based measurement systems (see Section I). For this reason, commercial geobrowsers, such as Google Earth, employ large-scale VHR satellite image databases whose entries are three-band images, in RGB true colors, that are not radiometrically calibrated [66]. This means that, if, in agreement with the QA4EO initiative, the radiometric calibration of spaceborne imagery becomes an RS data preprocessing requirement shared by all RS data applications, both scientific and recreational, then the automatic interpretation of RS images, e.g., the detection of man-made structures in VHR satellite images, can be made available to a vast public through commercial 3-D Earth viewers and geobrowsers.

ACKNOWLEDGMENT

The authors would like to thank the Editor-in-Chief, the Associate Editor, and the anonymous reviewers for their helpful comments and patience in reviewing this paper, as well as their competence and willingness to help.

REFERENCES

[1] [Online]. Available: www.fabricadebani.ro/userfiles/GEO_press_release.doc
[2] G. Gutman, A. C. Janetos, C. O. Justice, E. F. Moran, J. F. Mustard, R. R. Rindfuss, D. Skole, B. L. Turner, II, and M. A. Cochrane, Eds., *Land Change Science*. Dordrecht, The Netherlands: Kluwer, 2004.
[3] F. Sart, J. Inglada, R. Landry, and T. Pultz, "Risk management using remote sensing data: Moving from scientific to operational applications," in *Proc. SBSR Workshop*, Brasil, Apr. 23–27, 2001.
[4] O. Sjahputera, C. H. Davis, B. Claywell, N. J. Hudson, J. M. Keller, M. G. Vincent, Y. Li, M. Klaric, and C. R. Shyu, "GeoCDX: An automated change detection and exploitation system for high resolution satellite imagery," in *Proc. IGARSS*, Boston, MA, Jul. 6–11, 2008, pp. V-467–V-470, Paper FR4.101.1.
[5] GEO, "GEO 2007–2009 Work Plan: Toward Convergence," 2008. [Online]. Available: http://earthobservations.org
[6] GEO, "The Global Earth Observation System of Systems (GEOSS) 10-Year Implementation Plan," adopted Feb. 16, 2005. [Online]. Available: http://www.earthobservations.org/docs/10-Year%20Implementation%20Plan.pdf
[7] [Online]. Available: http://www.esa.int/esaLP/SEMOBSO4KKF_LPgmes_0.html
[8] [Online]. Available: http://www.gmes.info
[9] P. Zamperoni, "Plus ça va, moins ça va," *Pattern Recognit. Lett.*, vol. 17, no. 7, pp. 671–677, Jun. 1996.
[10] S. D'Elia, European Space Agency.
[11] *eCognition User Guide 4*, Definiens Imag. GmbH, Munich, Germany, 2004.
[12] R. Richter, "Atmospheric/Topographic Correction for Satellite Imagery—ATCOR-2/3 User Guide," 2006, ver. 6.2, DLR—German Aerospace Center, Remote Sensing Data Center, D—82234 Wessling/Germany, DLR-IB 565-01/06.
[13] M. Page-Jones, *The Practical Guide to Structured Systems Design*. Englewood Cliffs, NJ: Prentice-Hall, 1988.
[14] A. D. Tonchev and C. D. Tonchev, "Method for Measuring the Overall Operational Performance of Hydrocarbon Facilities." [Online]. Available: http://www.faqs.org/patents/app/20080262898
[15] W. Kaydos, *Operational Performance Measurement: Increasing Total Productivity*. Boca Raton, FL: CRC Press, 1999.
[16] A. Strahler, D. Muchoney, J. Borak, M. Friedl, S. Gopal, E. Lambin, and A. Moody, "Modis Land Cover Product Algorithm Theoretical Basis Document (ATBD)," MODIS Science Team, ver. 5.0. [Online]. Available: http://modis.gsfc.nasa.gov/data/atbd/atbd_mod12.pdf
[17] GEO/CEOSS, "A Quality Assurance Framework for Earth Observation," Sep. 2008, ver. 2.0. [Online]. Available: http://calvalportal.ceos.org/CalValPortal/showQA4EO.do?section=qa4eoIntro
[18] P. Mather, *Computer Processing of Remotely-Sensed Images—An Introduction*. Chichester, U.K.: Wiley, 1994.
[19] T. Matsuyama and V. S.-S. Hwang, *SIGMA—A Knowledge-Based Aerial Image Understanding System*. New York: Plenum, 1990.
[20] A. Baraldi, M. Gironda, and D. Simonetti, "Operational two-stage stratified topographic correction of spaceborne multi-spectral imagery employing a first-stage automatic spectral rule-based decision-tree classifier," *IEEE Trans. Geosci. Remote Sens.*, vol. 48, no. 1, pp. 112–146, Jan. 2010.
[21] A. K. Shackelford and C. H. Davis, "Fully automated road network extraction from high-resolution satellite multispectral imagery," in *Proc. IGARSS*, Toulouse, France, Jul. 2003, vol. 1, pp. 461–463.
[22] P. Soille, "On genuine connectivity relations based on logical predicates," in *Proc. 14th ICIAP*, Modena, Italy, 2007, pp. 487–492.
[23] F. Achard, R. DeFries, H. Eva, M. Hansen, P. Mayaux, and H.-J. Stibig, "Pan-tropical monitoring of deforestation," *Environ. Res. Lett.*, vol. 2, pp. 1–12, 2007.
[24] M. Herold, C. Woodcock, A. Di Gregorio, P. Mayaux, A. S. Belward, J. Latham, and C. Schmullius, "A joint initiative for harmonization and validation of land cover datasets," *IEEE Trans. Geosci. Remote Sens.*, vol. 44, no. 7, pp. 1719–1727, Jul. 2006.
[25] A. K. Shackelford and C. H. Davis, "A hierarchical fuzzy classification approach for high-resolution multispectral data over urban areas," *IEEE Trans. Geosci. Remote Sens.*, vol. 41, no. 9, pp. 1920–1932, Sep. 2003.
[26] A. K. Shackelford and C. H. Davis, "A combined fuzzy pixel-based and object-based approach for classification of high-resolution multispectral data over urban areas," *IEEE Trans. Geosci. Remote Sens.*, vol. 41, no. 10, pp. 2354–2363, Oct. 2003.
[27] A. Baraldi, V. Puzzolo, P. Blonda, L. Bruzzone, and C. Tarantino, "Automatic spectral rule-based preliminary mapping of calibrated Landsat TM and ETM+ images," *IEEE Trans. Geosci. Remote Sens.*, vol. 44, no. 9, pp. 2563–2586, Sep. 2006.
[28] M. Kathryn and M. Korenberg, "On the use of separable Volterra networks to model discrete-time Volterra systems," *IEEE Trans. Geosci. Remote Sens.*, vol. 12, no. 1, pp. 174–175, Jan. 2001.
[29] C. M. Bishop, *Neural Networks for Pattern Recognition*. Oxford, U.K.: Clarendon, 1995.
[30] A. Baraldi and F. Parmiggiani, "Combined detection of intensity and chromatic contours in color images," *Opt. Eng.*, vol. 35, no. 5, pp. 1413–1439, May 1996.
[31] A. Bharath and M. Petrou, *Next Generation Artificial Vision Systems—Reverse Engineering the Human Visual System*. Boston, MA: Artech House, 2008.
[32] J. Yang and R. S. Wang, "Classified road detection from satellite images based on perceptual organization," *Int. J. Remote Sens.*, vol. 28, no. 20, pp. 4653–4669, Oct. 2007.
[33] V. Cherkassky and F. Mulier, *Learning From Data: Concepts, Theory, and Methods*. New York: Wiley, 1998.
[34] *Image2000 and CORINE Land Cover (CLC) 2000*, Eur. Comm. Joint Res. Center, Brussels, Belgium, 2005, EUR 21757.
[35] E. Bartholome and A. Belward, "GLC2000: A new approach to global land cover mapping from earth observation data," *Int. J. Remote Sens.*, vol. 26, no. 9, pp. 1959–1977, May 2005.
[36] M. V. N. de Lima, C. Bielski, and C. Nowak, "IMAGE2006: A component of the GMES precursor fast track service on land monitoring," in *Proc. IGARSS*, Barcelona, Spain, Jul. 23–28, 2007, pp. 2669–2672.
[37] Z. G. Wei, A. P. Macwan, and P. A. Wieringa, "A quantitative measure for degree of automation and its relation to system performance and mental load," *Hum. Factors*, vol. 40, no. 2, pp. 277–295, Jun. 1998.
[38] P. Henry and A. Meygret, "Calibration of VEGETATION camera onboard SPOT4," *Adv. Space Res.*, vol. 28, no. 1, pp. 49–58, 2001.
[39] [Online]. Available: http://www.SPOTimage.fr/html/_167_224_584_.php
[40] D. Riaño, E. Chuvieco, J. Salas, and I. Aguado, "Assessment of different topographic corrections in Landsat TM data for mapping vegetation types," *IEEE Trans. Geosci. Remote Sens.*, vol. 41, no. 5, pp. 1056–1061, May 2003.
[41] [Online]. Available: http://eo1.usgs.gov
[42] T. Lillesand and R. Kiefer, *Remote Sensing and Image Interpretation*. New York: Wiley, 1994.
[43] P. S. Chavez, "An improved dark-object subtraction technique for atmospheric scattering correction of multispectral data," *Remote Sens. Environ.*, vol. 24, no. 3, pp. 459–479, Apr. 1988.

[44] D. Foldes and B. Benes, "Occlusion-based snow accumulation simulation," in *Proc. 4th Workshop VRIPHYS*, 2007, pp. 35–41.
[45] S. Liang, *Quantitative Remote Sensing of Land Surfaces*. Hoboken, NJ: Wiley, 2004.
[46] R. R. Irish, "Landsat 7 automatic cloud cover assessment (ACCA)," in *Proc. SPIE—Algorithms Multispectral, Hyperspectral, and Ultraspectral Imagery VI*, S. S. Shen and M. R. Descour, Eds., 2000, vol. 4049, pp. 348–355. [Online]. Available: ltpwww.gsfc.nasa.gov/IAS/handbook/pdfs/ACCA_SPIE_paper.pdf
[47] C. Small, "Multiresolution analysis of urban reflectance," in *Proc. IEEE/ISPRS Workshop, Data Fusion Over Urban Areas*, Rome, Italy, Nov. 2001, pp. 15–19.
[48] G. Zhou and M. Kafatos, "Future intelligent earth observing satellites (FIEOS)," in *Proc. ISPRS/FIEOS Conf.*, 2002. [Online]. Available: http://www.isprs.org/commission1/proceedings02/paper/00031.pdf
[49] [Online]. Available: http://directory.eoportal.org/info_3rdInternational-SymposiumonFutureIntelligentEarthObservingSatellitesFIEOS.html
[50] K. Pakzad, J. Bückner, and S. Growe, "Knowledge based moorland interpretation using a hybrid system for image analysis," in *Proc. ISPRS Conf.*, Munich, Germany, Sep. 8–10, 1999.
[51] P. Perona and J. Malik, "Scale-space and edge detection using anisotropic diffusion," *IEEE Trans. Pattern Anal. Mach. Intell.*, vol. 12, no. 7, pp. 629–639, Jul. 1990.
[52] S. T. Acton and J. Landis, "Multispectral anisotropic diffusion," *Int. J. Remote Sens.*, vol. 18, no. 13, pp. 2877–2886, Sep. 1997.
[53] J. Canny, "A computational approach to edge detection," *IEEE Trans. Pattern Anal. Mach. Intell.*, vol. PAMI-8, no. 6, pp. 679–698, Nov. 1986.
[54] A. Baraldi and F. Parmiggiani, "Single linkage region growing algorithms based on the vector degree of match," *IEEE Trans. Geosci. Remote Sens.*, vol. 34, no. 1, pp. 137–148, Jan. 1996.
[55] A. Baraldi and F. Parmiggiani, "A refined Gamma MAP SAR speckle filter with improved geometrical adaptivity," *IEEE Trans. Geosci. Remote Sens.*, vol. 33, no. 5, pp. 1245–1257, Sep. 1995.
[56] T. Lindeberg, "Detecting salient blob-like image structures and their scales with a scale-space primal sketch: A method for focus-of-attention," *Int. J. Comput. Vis.*, vol. 11, no. 3, pp. 283–318, Dec. 1993.
[57] C. Carson, S. Belongie, H. Greenspan, and J. Malik, "Region-based image querying," in *Proc. Int. Workshop Content-Based Access Image Video Libraries*, 1997, pp. 42–49.
[58] D. C. Burr and M. C. Morrone, "A nonlinear model of feature detection," in *Nonlinear Vision: Determination of Neural Receptive Fields, Functions, and Networks*, R. B. Pinter and N. Bahram, Eds. Boca Raton, FL: CRC Press, 1992, pp. 309–327.
[59] L. Delves, R. Wilkinson, C. Oliver, and R. White, "Comparing the performance of SAR image segmentation algorithms," *Int. J. Remote Sens.*, vol. 13, no. 11, pp. 2121–2149, 1992.
[60] G. J. Hay and G. Castilla, "Object-based image analysis: Strengths, weaknesses, opportunities and threats (SWOT)," in *Proc. 1st Int. Conf. OBIA*, S. Lang, T. Blaschke, and E. Schöpfer, Eds., 2006. [Online]. Available: www.commission4.isprs.org/obia06/Papers/01_Opening%20Session/OBIA2006_Hay_Castilla.pdf
[61] M. Nagao and T. Matsuyama, *A Structural Analysis of Complex Aerial Photographs*. New York: Plenum, 1980.
[62] R. A. Brooks, "Symbolic reasoning about 3-D models and 2-D images," *Artif. Intell.*, vol. 17, pp. 285–348, 1981.
[63] D. M. McKeown, W. A. Harvey, and J. McDermott, "Rule-based interpretation of aerial imagery," *IEEE Trans. Pattern Anal. Mach. Intell.*, vol. PAMI-7, no. 5, pp. 570–585, Sep. 1985.
[64] H. Niemann, G. Sagerer, S. Schroder, and F. Kummert, "ERNEST: A semantic network system for pattern understanding," *IEEE Trans. Pattern. Anal. Mach. Intell.*, vol. 12, no. 9, pp. 883–905, Sep. 1990.
[65] R. Serra and G. Zanarini, *Complex Systems and Cognitive Processes—The Dynamical Systems Approach to Artificial Intelligence*. Berlin, Germany: Springer-Verlag, 1990.
[66] A. Pekkarinen, L. Reithmaier, and P. Strobl, "Pan-European forest/non-forest mapping with Landsat ETM+ and CORINE Land Cover 2000 data," *ISPRS J. Photogramm. Remote Sens.*, vol. 64, no. 2, pp. 171–183, Mar. 2009.
[67] P. Corcoran and A. Winstanley, "Using texture to tackle the problem of scale in landcover classification," in *Object-Based Image Analysis—Spatial Concepts for Knowledge-Driven Remote Sensing Applications*, *Lecture Notes in Geoinformation and Cartography*, T. Blaschke, S. Lang, and G. Hay, Eds. Berlin, Germany: Springer-Verlag, 2007, pp. 113–132.
[68] D. Chakraborty and N. R. Pal, "A neuro-fuzzy scheme for simultaneous feature selection and fuzzy rule-based classification," *IEEE Trans. Neural Netw.*, vol. 15, no. 1, pp. 110–118, Jan. 2004.
[69] R. G. Congalton and K. Green, *Assessing the Accuracy of Remotely Sensed Data*. Boca Raton, FL: Lewis Publishers, 1999.
[70] [Online]. Available: http://www.coventry.ac.uk/ec/~nhunt/meths/strati.html
[71] A. Baraldi, L. Bruzzone, and P. Blonda, "Quality assessment of classification and cluster maps without ground truth knowledge," *IEEE Trans. Geosci. Remote Sens.*, vol. 43, no. 4, pp. 857–873, Apr. 2005.
[72] A. Baraldi, T. Wassenaar, and S. Kay, "Automatic preliminary spectral rule-based decision-tree classification of spaceborne very high resolution optical imagery—Mapping vegetation and bare soil types across European Union's agricultural landscapes," *IEEE Trans. Geosci. Remote Sens.*, 2009, to be published.
[73] ENVI 4.3 User Manual, ITT Industries Inc., Boulder, CO, 2006.
[74] Y. Sohn, E. Motan, and F. Gurri, "Deforestation in North-Central Yucatan (1985–1995): Mapping secondary succession of forest and agricultural land use in Sotuta using the cosine of the angle concept," *Photogramm. Eng. Remote Sens.*, vol. 65, no. 8, pp. 947–958, Aug. 1999.
[75] S. South, J. Qi, and D. P. Lusch, "Optimal classification methods for mapping agricultural tillage practices," *Remote Sens. Environ.*, vol. 91, no. 1, pp. 90–97, May 2004.
[76] J. A. Barsi, B. L. Markham, D. L. Helder, and G. Chander, "Radiometric calibration status of Landsat-7 and Landsat-5," in *Proc. SPIE*, 2007, vol. 6744, p. 674 41F. [Online]. Available: http://landsat.gsfc.nasa.gov/pdf_archive/publications/SPIE07_LandsatRadiometry.pdf
[77] C. H. Key and N. C. Benson, "Landscape assessment," USDA, Forest Service, Fort Collins, CO, 2006.
[78] [Online]. Available: http://www.esa.int/esaMI/Proba_web_site/ESARBKTHN6D_0.html
[79] L. A. Dupigny-Giroux and J. E. Lewis, "A moisture index for surface characterization over a semiarid area," *Photogramm. Eng. Remote Sens.*, vol. 65, no. 8, pp. 937–945, Aug. 1999.
[80] P. H. Swain and S. M. Davis, *Remote Sensing: The Quantitative Approach*. New York: McGraw-Hill, 1978.
[81] Personal communication, From: Stefano Natali [mailto:natali@meeo.it] Sent: Monday, Feb. 12, 2007 1:54 PM To: Casals, Vanessa Subject: SPOT DATA.
[82] G. Chander, B. L. Markham, and D. L. Helder, "Summary of current radiometric calibration coefficients for Landsat MSS, TM, ETM+, and EO-1 ALI sensors," *Remote Sens. Environ.*, vol. 113, no. 5, pp. 893–903, May 2009.
[83] IRS-P6 LGSOWG (Super Structure) Digital Data Products Format, Space Appl. Center, ISRO, Ahmedabad, India, May 2003. [Online]. Available: http://www.euromap.de/download/p6super_20050222.pdf
[84] A. Baraldi, "Impact of radiometric calibration and specifications of spaceborne optical imaging sensors on the development of operational automatic remote sensing image understanding systems," *IEEE J. Sel. Topics Appl. Earth Obs. Remote Sens.*, vol. 2, no. 2, pp. 104–134, Jun. 2009.
[85] [Online]. Available: http://www.mcst.ssai.biz/mcstweb/performance/aqua/aqua-swir-thermal.html
[86] GMES Image2006 Mosaic. [Online]. Available: http://www.gmes-gseland.info/com/news/GMES-Land_NewsLetter_I1.00.pdf
[87] K. W. Forsythe and P. Du, "Development patterns in Canada's largest urban agglomeration: Four decades of evolution," in *Proc. 1st EARSeL Workshop SIG Urban Remote Sens.*, Mar. 2–3, 2006. [Online]. Available: http://www.earsel.org/workshops/SIG-URS-2006/PDF/Session7_Forsythe.pdf
[88] A. Di Gregorio and L. Jansen, *Land Cover Classification System (LCCS): Classification Concepts and User Manual*, FAO: Rome, Italy, FAO Corporate Document Repository, 2000. [Online]. Available: http://www.fao.org/DOCREP/003/X0596E/X0596e00.htm
[89] B. C. Gao, "NDWI—A normalized difference water index for remote sensing of vegetation liquid water from space," *Remote Sens. Environ.*, vol. 58, no. 3, pp. 257–266, Dec. 1996.
[90] H. Xu, "Modification of normalized difference water index (NDWI) to enhance open water features in remotely sensed imagery," *Int. J. Remote Sens.*, vol. 27, no. 14, pp. 3025–3033, Jul. 2006.
[91] S. K. McFeeters, "The use of normalized difference water index (NDWI) in the delineation of open water features," *Int. J. Remote Sens.*, vol. 17, no. 7, pp. 1425–1432, May 1996.
[92] A. K. Shackelford and C. H. Davis, "A self-supervised approach for fully automated urban land cover classification of high resolution satellite imagery," in *Proc. 3rd Int. Symp. Remote Sens. Data Fusion Over Urban Areas—Urban*, Tempe, AZ, Mar. 14–16, 2005.
[93] [Online]. Available: http://landsaf.meteo.pt/
[94] [Online]. Available: http://services.eoportal.org/portal/system/AboutUsUI.jsp

[95] I. Couloigner, T. Ranchin, V. P. Valtonen, and L. Wald, "Benefit of the future SPOT-5 and of data fusion to urban roads mapping," *Int. J. Remote Sens.*, vol. 19, no. 8, pp. 1519–1532, May 1998.
[96] J. Ton, A. K. Jain, W. R. Enslin, and W. D. Hudson, "Automatic road identification and labeling in Landsat 4 TM images," *Photogrammetria*, vol. 43, pp. 257–276, 1989.
[97] C. Hudelot, J. Atif, and I. Bloch, "Fuzzy spatial relation ontology for image interpretation," *Fuzzy Sets Syst.*, vol. 159, no. 15, pp. 1929–1951, Aug. 2008.
[98] T. Esch, M. Thiel, M. Bock, A. Roth, and S. Dech, "Improvement of image segmentation accuracy based on multiscale optimization procedure," *IEEE Geosci. Remote Sens. Lett.*, vol. 5, no. 3, pp. 463–467, Jul. 2008.
[99] [Online]. Available: http://www.ceos.org
[100] I. Dowman, "Foreword," in *International Society for Photogrammetry and Remote Sensing (ISPRS) Book Series—Post-Launch Calibration of Satellite Sensors*, S. A. Morain and A. M. Buedge, Eds. Leiden, The Netherlands: A. A. Balkema Publishers, 2004, p. IX.
[101] C. Mason and E. R. Kandel, "Central visual pathways," in *Principles of Neural Science*, E. Kandel and J. Schwartz, Eds. Norwalk, CT: Appleton and Lange, 1991, pp. 420–439.
[102] P. Gouras, "Color vision," in *Principles of Neural Science*, E. Kandel and J. Schwartz, Eds. Norwalk, CT: Appleton and Lange, 1991, pp. 467–479.
[103] E. R. Kandel, "Perception of motion, depth and form," in *Principles of Neural Science*, E. Kandel and J. Schwartz, Eds. Norwalk, CT: Appleton and Lange, 1991, pp. 441–466.
[104] M. Petrou and P. Sevilla, *Image Processing: Dealing With Texture*. Chichester, U.K.: Wiley, 2006.
[105] K.-W. Park, J.-W. Jeong, and D.-H. Lee, "OLYBIA: Ontology-based automatic image annotation system using semantic inference rules," in *Advances in Databases: Concepts, Systems and Applications*. Berlin, Germany: Springer-Verlag, 2007, pp. 485–496.
[106] Q. Yu and D. A. Clausi, "SAR sea-ice image analysis based on iterative region growing using semantics," *IEEE Trans. Geosci. Remote Sens.*, vol. 45, no. 12, pp. 3919–3931, Dec. 2007.
[107] A. Belward, "Landsat Science Team Meeting," U.S. Forest Service, Fort Collins, CO, European Commission Joint Research Center Mission Report, Jan. 6–8, 2009.
[108] M. Craglia, M. Goodchild, A. Annoni, G. Camara, M. Gould, W. Kuhn, D. Mark, and I. Masser, "Next-generation digital earth—A position paper from the Vespucci initiative for the advancement of geographic information science," *Int. J. Spatial Data Infrastruct. Res.*, vol. 3, pp. 146–165, 2008.

Andrea Baraldi was born in Modena, Italy, in 1963. He received the "Laurea" (M.S.) degree in electronic engineering from the University of Bologna, Bologna, Italy, in 1989. His master thesis focused on the development of segmentation and classification algorithms for remotely sensed optical imagery.

From 1989 to 1990, he worked as a Research Associate with the Centro di Studio per l'Interazione Operatore-Calcolatore, Consiglio Nazionale Delle Ricerche (CNR), Bologna, and served in the army with the Istituto Geografico Militare, Florence, working on satellite image classifiers and geographic information systems (GIS). As a Consultant with the European Space Research Institute, European Space Agency, Frascati, Italy, he worked on object-oriented applications for GIS from 1991 to 1993. From December 1997 to June 1999, he was assigned with a postdoctoral fellowship in artificial intelligence with the International Computer Science Institute, Berkeley, CA. From 2000 to 2002, as a Postdoctoral Researcher, he joined the Global Vegetation Monitoring Unit, Institute for Environmental and Sustainability (IES), Joint Research Centre (JRC), European Commission, Ispra, Italy, where he worked on the development and validation of algorithms for forest classification of radar mosaics at continental scale. From 2005 to 2009, at the Spatial Data Infrastructure Unit, IES, he was involved with satellite optical image calibration, classification, and mosaicking at continental scale. Since his master thesis, he has continued his collaboration with Istituto di Scienze dell'Atmosfera e del Clima, CNR, Bologna and Instituto di Studi sui Sistemi Intelligenti per l'Automazione, CNR, Bari, Italy. He is currently with Baraldi Consultancy in Remote Sensing, Bologna. His main interests center on image understanding, with special emphasis on the development of operational automatic hierarchical multisource multiresolution spaceborne image understanding systems consistent with biological vision.

Mr. Baraldi served as an Associate Editor of the IEEE TRANSACTIONS ON NEURAL NETWORKS from 2001 to 2006.

Laurent Durieux received the Ph.D. degree in geography, with a specialization in remote sensing and geographic information systems, from the University of Aix-en-Provence, Aix-en-Provence, France.

He spent two years with the Aerospace Technical Center, Sao José dos Campos, Brazil, to study the impact of the deforestation on the convective clouds. Later, for two years, he was with the Global Vegetation Monitoring Unit, Joint Research Centre, Ispra, Italy, to develop Earth Observation techniques for global and regional vegetation mapping and monitoring with a particular emphasis on forest assessments. He is a Researcher with the "Institut de Recherche pour le Développement," Montpellier, France. He is actually the Coordinator of the Monitoring of the Environment Assisted by Satellite (SEAS, in French) program in Brazil and organizes the scientific cooperation with the Satellite Pour l'Observation de la Terre direct receiving antenna in Cayenne (French Guiana). His research interest focus on monitoring tropical land surface processes using data from Earth Observing satellites.

Dr. Durieux is the Vice President of the French Representation of the South-American Association of Remote Sensing.

Dario Simonetti was born in Varese, Italy, in 1981. He received the Laurea (M.S.) degree in informatics from the Universita' dell'Insubria, Facolta' di Scienze Matematiche, Fisiche e Naturali, Varese, in 2004. His thesis focused on the development of improved classification algorithms for near-real-time fire detection at global scale from satellite optical imagery.

He is currently with the Global Environment Monitoring Unit, Institute for Environment and Sustainability, Joint Research Centre, European Commission, Ispra, Italy, where he was an Analyst–Programmer Consultant from 2004 to 2009. His main activities are focused on: automatic near-real time analysis of fires occurrences in African protected areas; development and assessment of processing chain for calibration, coregistration, topographic correction, and classification of satellite imagery; and development of user-friendly geographic information systems application for validation of satellite imagery classification across different epochs. He is contributing in delivering products and services derived from the analysis of satellite remote sensing data, with special emphasis on biodiversity and land cover change detection.

Giulia Conchedda was born in Nuoro, Italy. She received the "Laurea" (M.S.) degree in tropical agriculture from the University of Florence, Florence, Italy, where she specialized in remote sensing and geographic information systems applied to the monitoring of natural resources in tropical countries, and the Ph.D. degree in geography from the University of Louvain-la-Neuve, Louvain-la-Neuve, Belgium.

As a Consultant in spatial, environment, and food security analysis in Africa and Latin America countries, she has been working for several international organizations for more than ten years. She is currently with the European Commission, Brussels, Belgium.

Francesco Holecz received the M.Sc. degree in geography and the Ph.D. degree in remote sensing from the Remote Sensing Laboratories, Institute of Geography, University of Zurich, Zurich, Switzerland, in 1985 and 1993, respectively.

From 1994 to 1996, he was a Visiting Scientist with the Radar Sciences and Engineering Section, NASA Jet Propulsion Laboratory, where his research focused on synthetic aperture radar (SAR) data calibration, polarimetry, and estimation of forest biomass using low-frequency polarimetric SAR data. From 1996 to 1999, he was a Research Scientist with the Remote Sensing Laboratories, Institute of Geography, University of Zurich, working on the development of an airborne X- and P-band interferometric SAR processor and spaceborne SAR applications in the domain of agriculture, forestry, and snow. As cofounder of Sarmap s.a., Purasca, Switzerland, he has been working as CEO of Sarmap s.a. since 1998. His main interests focus on the development of SAR and optical multispectral image understanding algorithms for automatic mapping and inference of biophysical parameters.

Palma Blonda (M'93) received the Ph.D. degree in physics from the University of Bari, Bari, Italy, in 1980.

In 1984, she joined the Institute for Signal and Image Processing, Italian National Research Council, Bari, which has recently changed its name as the Instituto di Studi sui Sistemi Intelligenti per I'Automazione. Her research interests include digital image processing, fuzzy logic, neural networks, and soft computing applied to multisource remotely sensed data fusion and classification. She was recently involved with the project "Landslide Early Warning Integrated System (LEWIS)," EVG1-CT-2001-00055, funded by the European Community in the context of the Fifth Program Framework, where her research interests focused on multisource data fusion and classification techniques for the extraction of superficial changes of landslide-related factors observable from space.

Dr. Blonda is a member of the IEEE society.